Angular-momentum projection in coupled-cluster theory: Structure of ^{34}Mg

G. Hagen, S. J. Novario,* Z. H. Sun, and T. Papenbrock
Physics Division, Oak Ridge National Laboratory, Oak Ridge, Tennessee 37831, USA
and Department of Physics and Astronomy, University of Tennessee, Knoxville, Tennessee 37996, USA

G. R. Jansen
National Center for Computational Sciences, Oak Ridge National Laboratory, Oak Ridge, Tennessee 37831, USA
and Physics Division, Oak Ridge National Laboratory, Oak Ridge, Tennessee 37831, USA

J. G. Lietz
National Center for Computational Sciences, Oak Ridge National Laboratory, Oak Ridge, Tennessee 37831, USA

T. Duguet
IRFU, CEA, Université Paris-Saclay, F-91191 Gif-sur-Yvette, France
and KU Leuven, Instituut voor Kern- en Stralingsfysica, 3001 Leuven, Belgium

A. Tichai
Institut für Kernphysik, Technische Universität Darmstadt, Department of Physics, 64289 Darmstadt, Germany;
Max-Planck-Institut für Kernphysik, Saupfercheckweg 1, 69117 Heidelberg, Germany;
and ExtreMe Matter Institute EMMI, GSI Helmholtzzentrum für Schwerionenforschung GmbH, 64291 Darmstadt, Germany

(Received 20 January 2022; accepted 7 June 2022; published 23 June 2022)

Single- reference coupled-cluster theory is an accurate and affordable computational method for the nuclear many-body problem. For open-shell nuclei, the reference state typically breaks rotational invariance and angular momentum must be restored as a good quantum number. We perform angular-momentum projection after variation and employ the disentangled coupled-cluster formalism and a Hermitian approach. We compare our results with benchmarks for ^{8}Be and ^{20}Ne using a two-nucleon interaction from chiral effective field theory and for pf-shell nuclei within the traditional shell model. We compute the rotational band in the exotic nucleus ^{34}Mg and find agreement with data.

DOI: 10.1103/PhysRevC.105.064311

I. INTRODUCTION

While angular momentum, parity, and the numbers of neutrons and protons are good quantum numbers of atomic nuclei, mean-field states often break symmetries of the nuclear Hamiltonian [1–3]. This is a blessing and a burden: On the one hand, the actual breaking of symmetries by the mean field corresponds to the emergent symmetry breaking in atomic nuclei; it informs us about deformation and superfluidity (in the case of breaking of angular momentum and particle numbers, respectively) and identifies the corresponding Nambu-Goldstone modes as low-energy degrees of freedom. Symmetry-breaking product states also are the starting point of single-reference methods (such as coupled-cluster theory [4,5], in-medium similarity renormalization group [6–11], Green's function and/or Gorkov approaches [12,13], and perturbation theory [14–19]) that capture dynamical correlations beyond the mean field [17,20,21]. On the other hand, the restoration of broken symmetries is necessary when one wants to obtain precise ground-state energies, excited states, or transition matrix elements between states with definite quantum numbers.

One can, of course, address phenomena related to emergent symmetry breaking without actually breaking any symmetry [22–28]. However, such exact computations typically scale exponentially with increasing number of active nucleons because the emergence of a new low-energy scale associated with, e.g., collective rotational excitations in intrinsically deformed nuclei requires the superposition of A-particle–A-hole excitations in a nucleus with mass number A. The successful computation of such states is then limited to light nuclei or small shell-model spaces. Monte Carlo methods with angular momentum projection extended such computations to somewhat larger model spaces [29]. In contrast, symmetry-adapted approaches [30,31] and effective theories [32–36] are simpler because they employ the degrees of freedom that are relevant at such low energies. The effective theories have advantages and disadvantages: they have less predictive power because

*Present address: Theoretical Division, Los Alamos National Laboratory, Los Alamos, New Mexico 87545, USA.

low-energy constants such as the moment of inertia, for instance, must be taken from data or microscopic computations. However, they allow us to estimate uncertainties and reveal the simple patterns that complex systems exhibit based on their symmetries and symmetry breaking.

While nuclear density-functional theory has been the main workhorse to compute nuclei across the nuclear chart [2,37–41], polynomially scaling computational methods [5,7,12,19] based on nucleon-nucleon and three-nucleon interactions from effective field theories of quantum chromodynamics [42–44] are advancing steadily towards heavier nuclei [10,20,45–48]. In this paper we employ single-reference coupled-cluster theory [4,5,49], start from a deformed but axially symmetric reference state [20], and perform angular momentum projection. Alternative methods for angular momentum projection are the multireference in-medium similarity renormalization group method [50] and many-body perturbation theory based on a reference state obtained via the projected generator coordinate method [51–53].

Several works discuss symmetry projection within coupled-cluster theory [54–60]. In particular the disentangled cluster formalism of Refs. [55,57,58] performs angular-momentum and particle-number projections. Here, the simplest approach is to insert the projected coupled-cluster state into the Schrödinger equation and project from the left onto the symmetry-broken reference state. In standard coupled-cluster theory, however, one would start from a bivariational energy functional of the projected Hamiltonian, where the bra state consists of a linear superposition of particle-hole excitations [49]. Such an approach is more accurate in general [55]. In both approaches the energy expression is non-Hermitian and the ket state is the usual exponential wave function ansatz.

There are coupled-cluster methods where the bra state is treated more on equal footing with the ket state, such as the extended coupled-cluster [61,62], the quadratic coupled-cluster [63,64], the expectation-value coupled-cluster [65], and the variational coupled-cluster [66] methods. While these methods are more accurate than the standard coupled-cluster method they come at a significantly higher computational cost. In this work we also follow a middle way using a Hermitian energy functional in the projection, inspired by the variational coupled-cluster method [66]. In this approach the rotation operator can be treated exactly but the exponential coupled-cluster state must be truncated.

This paper is organized as follows. In Sec. II we discuss the role of static and dynamical correlations in angular momentum projection. Section III introduces the coupled-cluster method and discusses reference states. In Sec. IV we present the theoretical derivations of angular-momentum projections after variation. Here, both the non-Hermitian and Hermitian projection methods will be described. In Sec. V we construct collective Hamiltonians within an effective theory and discuss the resolution-scale dependence and size consistency in projections. In Sec. VI we show results for angular-momentum projection of the nuclei ^{8}Be, ^{20}Ne, and ^{34}Mg. Section VII deals with angular momentum projection of coupled-cluster computations in the traditional shell model. We present a discussion and summary in Sec. VIII.

II. STATIC AND DYNAMICAL CORRELATIONS

The restoration of rotational symmetry of a nucleus with mass number A involves A-particle–A-hole (Ap-Ah) excitations, because it requires the rotation of a deformed nucleus. This makes it challenging to keep size extensivity [67] together with computational affordability. Fortunately, the problem is somewhat less daunting, because the computation of a nuclear ground-state energy involves dynamic and nondynamic (or static) correlations; see, e.g., Ref. [68] for a recent discussion of this topic.

Dynamic correlations mix a dominant configuration and a large number of configurations carrying small individual weights but yielding a significant energy contribution. An example is provided by the dominant (symmetry breaking) Hartree-Fock reference state and its 2p-2h and 3p-3h excitations. While the number of relevant configurations is large, it only grows polynomially with mass number and model-space size for any targeted precision. As dynamical correlations bring in the lion's share of nuclear binding, one needs size-extensive methods to capture them accurately.

In contrast, static correlations are caused by a number of equally important configurations. Any rotation of a deformed reference state, for example, yields a configuration that is degenerate in energy. Mixing these states, e.g., via angular momentum projection, lowers the rotational zero-point energy. As we will see below, this energy gain decreases with increasing mass number. For heavy deformed nuclei the energy gain from projection is of the order of the nuclear level spacing near the ground state.

Based on this discussion, we can decompose the ground-state energy as

$$E = E_{\mathrm{ref}} + \Delta E + \delta E. \tag{1}$$

Here E_{ref}, ΔE, and δE denote the energy of the symmetry-breaking reference state, the energy associated with dynamical correlations and the static energy from angular momentum restoration, respectively. These energies scale as $E_{\mathrm{ref}} \propto A$, $\Delta E \propto A$ and as $\delta E \propto A^{-\eta}$ where $\eta > 0$. We estimate that $\eta \approx 1/6$, based on the scaling $\delta E \sim \langle J^2 \rangle / \Theta$ where $\Theta \sim A^{5/3}$ expresses the scaling of the moment of inertia and $\langle J^2 \rangle \sim A^{3/2}$ is the scaling of the angular momentum for the unprojected reference state found empirically in projected mean-field calculations [69]. Because of its smallness and scaling with A, one does not need size-extensive methods to compute δE. In contrast, we compute E_{ref} and ΔE via the symmetry-breaking and size-extensive Hartree-Fock and coupled-cluster methods, respectively.

III. COUPLED-CLUSTER METHOD AND REFERENCE STATES

We use single-particle states $|p\rangle$ where $p = (n, \pi, j_z, t_z)$ denotes a quantum number n, parity π, angular momentum projection j_z, and isospin projection t_z. We have $|p\rangle \equiv c_p^\dagger |0\rangle$ where $|0\rangle$ is the vacuum and $c_p^\dagger$ creates a nucleon. The creation operators and corresponding annihilation operators c_p obey the usual anticommutation relations for fermions.

The Hamiltonian is

$$H = \sum_{pq} \varepsilon_{pq} c_p^\dagger c_q + \frac{1}{4} \sum_{pqrs} v_{pqrs} c_p^\dagger c_q^\dagger c_s c_r. \tag{2}$$

While three-nucleon forces are unavoidable in nuclear physics [70–73], we omitted them for simplicity and to benchmark with other methods that employ the same interaction.

Our calculations start from the symmetry-unrestricted product state

$$|\Phi\rangle \equiv \prod_{i=1}^{A} c_i^\dagger |0\rangle. \tag{3}$$

This state breaks angular momentum but we assume that its projection J_z is conserved. We also assume that parity, isospin projection, and mass number A are conserved, and that we deal with even-even nuclei. Then, the reference $|\Phi\rangle$ is also invariant under time reversal (and occupied single-particle states come in degenerate Kramer pairs), invariant under rotations by an angle π around any axis that is perpendicular to the symmetry axis (denoted as $\mathcal{R}$ parity [74]), and fulfills $J_z|\Phi\rangle = 0$.

We discuss three choices for the reference state. The Hartree-Fock state, which minimizes the energy, is the first. The second reference is obtained as follows. We minimize the energy under the constraint of a fixed expectation value q_{20} of the mass quadrupole operator

$$Q_{20} = \sqrt{\frac{16\pi}{5}} \sum_{i=1}^{A} r_i^2 Y_{20}(\theta_i, \phi_i). \tag{4}$$

Such a constrained Hartree-Fock calculation employs the Routhian

$$R \equiv H - \lambda Q_{20}, \tag{5}$$

where the Lagrange multiplier λ is adjusted to obtain the desired value $q_{20} = \langle Q_{20} \rangle$. We use the augmented Lagrangian method [75] for this purpose and generate an energy curve as a function q_{20}. Performing an angular-momentum projection after variation at fixed q_{20} then yields a new curve whose minimum we seek. The corresponding product state is the Hartree-Fock restricted-variation-after-projection (HF-RVAP) reference [76,77]. The third reference state is obtained from a variation-after-projection Hartree-Fock (HF-VAP) calculation [78,79]. The HF-VAP reference state constitutes the optimal (i.e., lowest energy) product state that can be obtained while including the projection onto zero angular momentum.

We note that the HF-VAP solution is obtained via the minimization of the projected energy over the complete manifold of Slater determinants. In contrast, the HF-RVAP solution is obtained via the minimization of the projected energy over the restricted manifold of Slater determinants generated through a set of constrained HF calculations. If the manifold spanned via the constrained HF calculation generates the complete set of Slater determinants, the HF-RVAP solution actually equals the HF-VAP solution. This clarifies the connection between the two approaches and explains the name HF-RVAP.

Once the single-particle basis is determined we normal order the Hamiltonian (7) with respect to the vacuum state and write

$$H = E_{\rm ref} + H_N. \tag{6}$$

Here, $E_{\rm ref} = \langle \Phi | H | \Phi \rangle = \sum_{i=1}^{A} \varepsilon_{ii} + \frac{1}{2} \sum_{i,j=1}^{A} v_{ijij}$ is the vacuum energy and the normal-ordered Hamiltonian is

$$H_N = \sum_{pq} f_{pq} \{c_p^\dagger c_q\} + \frac{1}{4} \sum_{pqrs} v_{pqrs} \{c_p^\dagger c_q^\dagger c_s c_r\}. \tag{7}$$

The curly brackets denote normal ordering and the Fock-matrix elements are $f_{pq} = \varepsilon_{pq} + \sum_{i=1}^{A} v_{piqi}$. The papers [80,81] proposed how to deal with three-body forces in the normal-ordered two-body approximation [82,83] in symmetry-breaking situations.

Coupled-cluster theory parametrizes the ground state as

$$|\Psi\rangle \equiv e^T |\Phi\rangle. \tag{8}$$

The cluster operator

$$T \equiv T_1 + T_2 + \cdots + T_A \tag{9}$$

consists of np-nh excitation operators

$$T_n = \frac{1}{(n!)^2} \sum_{\substack{a_1,\ldots,a_n \\ i_1,\ldots,i_n}} t_{i_1,\ldots,i_n}^{a_1,\ldots,a_n} c_{a_1}^\dagger \cdots c_{a_n}^\dagger c_{i_n} \cdots c_{i_1}. \tag{10}$$

Here and in what follows, $i, j, k, \ldots$ label occupied single-particle states while $a, b, c, \ldots$ refer to unoccupied states. Generic states are labeled as $p, q, r, \ldots$. Coupled-cluster theory is a powerful method because the numerically inexpensive singles and doubles (CCSD) approximation $T \approx T_1 + T_2$ yields about 90% of the correlation energy for closed-shell nuclei; the inclusion of triples $T = T_1 + T_2 + T_3$, still numerically affordable via perturbative methods, yields about 98%. In CCSD, the cluster amplitudes are computed for a given Hamiltonian and reference state by solving the well-known coupled-cluster equations [84]

$$\begin{aligned} \langle \Phi_i^a | e^{-T} H_N e^T | \Phi \rangle &= 0, \\ \langle \Phi_{ij}^{ab} | e^{-T} H_N e^T | \Phi \rangle &= 0. \end{aligned} \tag{11}$$

Here, $|\Phi_{i_1\cdots i_n}^{a_1\cdots a_n}\rangle \equiv c_{a_1}^\dagger \cdots c_{a_n}^\dagger c_{i_n} \cdots c_{i_1} |\Phi\rangle$ is a np-nh excitation of the reference state. The energy associated with the (dynamical) CCSD correlations is

$$\Delta E_{\rm CCSD} = \langle \Phi | e^{-T} H_N e^T | \Phi \rangle. \tag{12}$$

As $\langle \Phi | e^{-T} = \langle \Phi |$ and $\langle \Phi | \Psi \rangle = 1$ we can rewrite the total energy as

$$E = E_{\rm ref} + \Delta E_{\rm CCSD} = \frac{\langle \Phi | H | \Psi \rangle}{\langle \Phi | \Psi \rangle}. \tag{13}$$

This energy expression will be modified below for the evaluation of the static correlation energy (δE) associated with angular-momentum projection.

For any truncation of the cluster operator the state $|\Psi\rangle$ breaks the same symmetries as the reference state $|\Phi\rangle$. Only the full expansion (9) restores the symmetries broken by the reference. In what follows we restore the rotational invariance via angular-momentum projection. In addition to CCSD, we will also use the CCD approximation $T = T_2$. In the Hartree-Fock basis there is little difference between CCD and CCSD

(because singles excitations are small). This is different in other single-particle bases.

The angular momentum projection methods we employ come at a considerable higher computational cost compared to the unprojected coupled-cluster calculations, and thus require us to work in smaller model spaces. The residual basis dependence can to a large extent be eliminated by including the singles-excitations in the projection, i.e., by using CCSD rather than CCD. In this work we also employ a natural-orbital basis obtained from second-order many-body perturbation theory [20,85]. In this approach we compute the Hartree-Fock state in a large harmonic oscillator basis, and in a final step truncate the normal-ordered Hamiltonian that enter the coupled-cluster computations to a smaller model space [86,87]. This alleviates the dependence on the oscillator frequency. We note, however, that such a truncation of the normal-ordered Hamiltonian breaks rotational invariance to a small extent.

IV. ANGULAR MOMENTUM PROJECTION

Throughout this section we use the Hamiltonian in the form of Eq. (6) [rather than Eq. (7)] because this facilitates the evaluation of the matrix elements we need to compute within the angular momentum projection.

A. Projection operator

The operator

$$P_J = \frac{1}{2}\int_0^\pi d\beta \sin\beta d^J_{00}(\beta) R(\beta), \tag{14}$$

projects a state with $J_z = 0$ onto total angular momentum J. Here,

$$R(\beta) \equiv e^{-i\beta J_y} \tag{15}$$

denotes the operator that rotates by the angle β around the y axis, and $d^J_{MK}(\beta)$ is related to the Wigner D function via [88]

$$D^J_{MK}(\alpha,\beta,\gamma) \equiv e^{-iM\alpha} d^J_{MK}(\beta) e^{-iK\gamma}. \tag{16}$$

The $\mathcal{R}$ symmetry allows us to restrict the domain of integration in Eq. (14) to the interval $[0, \pi/2]$ because

$$R(\pi-\beta)|\Phi\rangle = R(\beta)|\Phi\rangle. \tag{17}$$

In a spherical single-particle basis $\{|p\rangle \equiv |\alpha_p j_p m_p\rangle\}$ of the one-body Hilbert space, matrix elements of the rotation operator are given by

$$\langle \alpha_p j_p m_p | R(\beta) | \alpha_q j_q m_q\rangle = \delta_{\alpha_p\alpha_q}\delta_{j_p j_q} d^{j_p}_{m_p m_q}(\beta). \tag{18}$$

B. Non-Hermitian projection formalism

1. Projected energy

The disentangled cluster formalism [55,57,58] (in its simplest implementation) is based on the standard non-Hermitian energy expression of coupled-cluster theory. In this approach the energy projected onto angular momentum J after variation is

$$E^{(J)} \equiv \frac{\langle\Phi|P_J H|\Psi\rangle}{\langle\Phi|P_J|\Psi\rangle}. \tag{19}$$

In this expression we used that P_J commutes with H. The projected energy is a natural modification of Eq. (13). We insert Eq. (14) into Eq. (19) and find

$$E^{(J)} = \frac{\int_0^\pi d\beta \sin\beta d^J_{00}(\beta)\mathcal{H}(\beta)}{\int_0^\pi d\beta \sin\beta d^J_{00}(\beta)\mathcal{N}(\beta)}. \tag{20}$$

Here,

$$\mathcal{N}(\beta) \equiv \langle\Phi|R(\beta)|\Psi\rangle \tag{21}$$

and

$$\mathcal{H}(\beta) \equiv \langle\Phi|R(\beta)H|\Psi\rangle \tag{22}$$

are the norm and Hamiltonian kernels, respectively. The $\mathcal{R}$ symmetry implies

$$\begin{aligned}\mathcal{N}(\pi-\beta) &= \mathcal{N}(\beta),\\ \mathcal{H}(\pi-\beta) &= \mathcal{H}(\beta).\end{aligned} \tag{23}$$

We also have $\mathcal{H}(0) = E_{\rm ref} + \Delta E$ and $\mathcal{N}(0) = 1$. Using Eq. (1) the static correlation energy associated with angular momentum projection is then $\delta E = E^{(0)} - E$.

2. Disentangled cluster formalism

Thouless's theorem [89] allows us to write [55]

$$\langle\Phi|R(\beta) = \langle\Phi|R(\beta)|\Phi\rangle\langle\Phi|e^{V(\beta)}. \tag{24}$$

Here the deexcitation operator is

$$V(\beta) = \sum_{ia} V^i_a(\beta) c^\dagger_i c_a. \tag{25}$$

Expressions for the matrix elements V^i_a and mean-field norm kernel $\langle\Phi|R(\beta)|\Phi\rangle$ can be found in Ref. [55]. In what follows we suppress the explicit dependence of various quantities, e.g., $V(\beta)$, on the angle β.

By virtue of Eq. (24) the kernels become

$$\mathcal{N}(\beta) = \langle\Phi|R(\beta)|\Phi\rangle\langle\Phi|e^V e^T|\Phi\rangle, \tag{26a}$$

$$\mathcal{H}(\beta) = \langle\Phi|R(\beta)|\Phi\rangle\langle\Phi|e^V H e^T|\Phi\rangle, \tag{26b}$$

and we are left with the evaluation of the reduced kernels

$$n(\beta) \equiv \langle\Phi|e^V e^T|\Phi\rangle, \tag{27a}$$

$$h(\beta) \equiv \langle\Phi|e^V H e^T|\Phi\rangle. \tag{27b}$$

Inserting the identity operator $1 = e^{-V}e^V$ introduces the similarity transformation [54,55]

$$\overline{H} \equiv e^V H e^{-V}. \tag{28}$$

As V is a one-body operator, $\overline{H}$ has the same particle rank as H, i.e., no many-body forces of higher rank are induced by the similarity transformation. In contrast to H, the operator $\overline{H}$ does not commute with J_z and this significantly increases the number of nonzero matrix elements that need to be stored. Using $\overline{H}$ yields

$$h(\beta) = \langle\Phi|\overline{H}e^V e^T|\Phi\rangle. \tag{29}$$

The exact evaluation of $e^V e^T$ in Eq. (29) is exponentially expensive. To make progress we introduce the disentangled

cluster operator

$$W(\beta) = W_0 + W_1 + W_2 + \cdots + W_A \tag{30}$$

via

$$e^V e^T |\Phi\rangle \equiv e^{W_0+W_1+W_2+\cdots}|\Phi\rangle. \tag{31}$$

Here W_k is a k-body excitation operator. In contrast to T, the operator $W(\beta)$ also contains a zero-body term $W_0(\beta)$. Even if T is truncated within the CCSD approximation $T = T_1 + T_2$, the operator $W(\beta)$ contains up to A-body operators. To keep the computation affordable one needs to truncate at some rank $k \ll A$. Then neither e^V nor e^T are exactly contained in the truncated e^W (note, however, that e^{T_1} will be treated exactly as it only amounts to a rotation of the basis, as will be shown below). As a consequence the $\mathcal{R}$ symmetry of the kernels [see Eq. (23)] is lost and the projection of the Hamiltonian $H = a\hat{J}^2$ only leads to approximate values $E^{(J)} \approx aJ(J+1)$. As we will see below, however, the disentangled approach is quite accurate. The truncation is a controlled approximation and can be systematically improved.

The matrix elements of the operator $W(\beta)$ are computed by solving the following set of ordinary differential equations:[1]

$$\begin{aligned}
\frac{d}{d\beta}W_0 &= X_a^i W_i^a, \\
\frac{d}{d\beta}W_i^a &= X_c^k\left(W_{ik}^{ac} - W_k^a W_i^c\right), \\
\frac{d}{d\beta}W_{ij}^{ab} &= X_c^k\left[W_{ijk}^{abc} - P(ij)W_{kj}^{ab}W_i^c - P(ab)W_{ij}^{cb}W_k^a\right], \\
&\vdots
\end{aligned} \tag{32}$$

where

$$X_a^i \equiv \left(\frac{dV}{d\beta}\right)_a^i, \tag{33}$$

and where $P(ab)$ denotes the permutation operator. Expressions of the matrix elements X_i^a can be found in Ref. [55]. The initial conditions for $\beta = 0$ are $W_0(0) = 0$ and $W_k(0) = T_k$ for all k.

3. Approximation schemes

In this work we truncate $W = W_0 + W_1 + W_2$ at the two-body level. The Baker-Campbell-Hausdorff expansion yields

$$n(\beta) = e^{W_0}, \tag{34a}$$

$$h(\beta) = e^{W_0}\langle\Phi|\overline{H}\left(1 + W_1 + W_2 + \frac{W_1^2}{2}\right)|\Phi\rangle. \tag{34b}$$

In Ref. [55] the disentangled formalism was developed for the coupled-cluster doubles (CCD) approximation $T = T_2$. Those authors noted that the extension to $T = T_1 + T_2$ could be achieved by inserting the identity $e^{T_1}e^{-T_1}$ to the left and right of the rotation operator in the original expression of the approximate kernels such that

$$\mathcal{N}(\beta) \equiv \langle\Phi|\check{R}(\beta)e^{T_2}|\Phi\rangle, \tag{35a}$$

$$\mathcal{H}(\beta) \equiv \langle\Phi|\check{R}(\beta)\check{H}e^{T_2}|\Phi\rangle. \tag{35b}$$

Here the similarly transformed operator

$$\check{O} \equiv e^{-T_1}Oe^{T_1} \tag{36}$$

amounts to a change of the single-particle basis. Given the form of the approximate kernels in Eq. (35), all equations at play for $T = T_2$ can be reused by substituting $R(\beta)$ and H by $\check{R}(\beta)$ and $\check{H}$, respectively, and by using $W_1(\beta = 0) = 0$ as the initial condition. We checked that the two equivalent ways to include T_1 lead to identical results.

C. Hermitian projection formalism

1. Projected energy

The Hermitian ansatz for the projected-after-variation (PAV) energy functional

$$E^{(J)} = \frac{\langle\Psi|P_J H|\Psi\rangle}{\langle\Psi|P_J|\Psi\rangle}, \tag{37}$$

where $|\Psi\rangle$ is the coupled-cluster state (8), can be rewritten as

$$E^{(J)} = \frac{\int_0^{\pi/2} d\beta \sin\beta d_{00}^J(\beta)\mathcal{H}_H(\beta)}{\int_0^{\pi/2} d\beta \sin\beta d_{00}^J(\beta)\mathcal{N}_H(\beta)}, \tag{38}$$

using the norm and Hamiltonian kernels

$$\begin{aligned}
\mathcal{N}_H(\beta) &\equiv \langle\Psi|R(\beta)|\Psi\rangle, \\
\mathcal{H}_H(\beta) &\equiv \langle\Psi|R(\beta)H|\Psi\rangle.
\end{aligned} \tag{39}$$

As in the non-Hermitian case, the coupled-cluster energy is recovered in absence of the projector [84].

2. Approximation schemes

In the following the coupled-cluster state (8) is truncated at the CCSD level, $T = T_1 + T_2$. Because of the exponential ansatz in the bra and ket, the exact evaluation of the projected energy (37) is not feasible and we need to make an approximation. We truncate the power series of e^{T_2} term by its first three terms and approximate $|\Psi\rangle$ as

$$|\Psi_{\text{SQD}}\rangle \equiv e^{T_1}\left(1 + T_2 + \tfrac{1}{2}T_2^2\right)|\Phi\rangle, \tag{40}$$

which leads to the singles quadratic doubles (SQD) approximation. Further dropping the T_2^2 term leads to the singles linear doubles (SLD) approximation

$$|\Psi_{\text{SLD}}\rangle \equiv e^{T_1}(1 + T_2)|\Phi\rangle. \tag{41}$$

The SLD and SQD approximations are attractive because they treat the rotation $R(\beta)$ and $\exp(T_1)$ exactly via similarity transformations. This approach is similar to the spin-extended formalism of Ref. [59]. The SLD ansatz is computationally inexpensive because it neglects the T_2^2 term.

3. Amplitude equations

The symmetry-breaking amplitudes t_i^a and t_{ij}^{ab} employed in the SQD approximation (40) are obtained by left-projecting

[1] Equation (32) corrects typographical errors found in Ref. [55].

the Schrödinger equation onto 1p-1h and 2p-2h excitations of the reference state; this yields

$$\langle \Phi_i^a | (H-E) e^{T_1} \left(1 + T_2 + \tfrac{1}{2}T_2^2\right) | \Phi \rangle = 0, \tag{42a}$$

$$\langle \Phi_{ij}^{ab} | (H-E) e^{T_1} \left(1 + T_2 + t\tfrac{1}{2}T_2^2\right) | \Phi \rangle = 0, \tag{42b}$$

$$E = \langle \Phi | H e^{T_1} \left(1 + T_2 + \tfrac{1}{2}T_2^2\right) | \Phi \rangle. \tag{43}$$

These are the standard CCSD equations. In the SLD approximation, the amplitudes are obtained from solving a configuration interaction problem truncated at doubles excitations starting from $\breve{H}$, i.e.,

$$\breve{H}(1 + T_2)|\Phi\rangle = E(1 + T_2)|\Phi\rangle, \tag{44}$$

and projecting from the left with $\langle \Phi_{ij}^{ab}|$ we obtain a linear problem in T_2 that can be solved iteratively. In contrast to SQD (or CCSD), the SLD approach is variational but not size extensive. Due to the lack of size extensivity the SLD (dynamical) correlation energy will not be accurate for ^{20}Ne and ^{34}Mg, but the SLD energy gain (δE_{SLD}) from angular-momentum projection can accurately be computed with methods that lack size extensivity since it is small and decreases with increasing mass.

4. Hamiltonian and norm kernels

The norm and Hamiltonian kernels (39) are

$$\mathcal{N}_H(\beta) \equiv \langle \Phi | U^\dagger e^{T_1^\dagger} R(\beta) e^{T_1} U | \Phi \rangle, \tag{45a}$$

$$\mathcal{H}_H(\beta) \equiv \langle \Phi | U^\dagger e^{T_1^\dagger} R(\beta) H e^{T_1} U | \Phi \rangle. \tag{45b}$$

Here we introduced the excitation operator

$$U \equiv 1 + T_2 + \tfrac{1}{2}T_2^2. \tag{46}$$

We note that for the SQD approach $\mathcal{H}_H(0)/\mathcal{N}_H(0) \neq E_{\rm SQD}$, and that $\mathcal{H}_H(0)/\mathcal{N}_H(0) > E_{\rm SQD}$ because the Hermitian approach lacks size extensivity when the exponential e^T is truncated. Nevertheless, the Hermitian approach is useful to compute energy differences $E^{(J)} - E^{(0)}$ and the energy gain $\delta E = E^{(0)} - \mathcal{H}_H(0)$ from angular-momentum projection because the magnitudes of these quantities decrease with increasing mass number.

Focusing first on the Hamiltonian kernel and inserting $1 = \exp(T_1)\exp(-T_1)$ allows us to rewrite

$$\mathcal{H}_H(\beta) = \langle \Phi | U^\dagger \mathcal{R}(\beta) \breve{H} U | \Phi \rangle. \tag{47}$$

Here

$$\mathcal{R}(\beta) \equiv e^{T_1^\dagger} R(\beta) e^{T_1} \tag{48}$$

is a product of exponentiated one-body operators, each of which induces a transformation of the single-particle basis that can be handled exactly.

Inserting the identity $\mathcal{R}(\beta)\mathcal{R}^{-1}(\beta)$ and using Thouless's theorem leads to

$$\mathcal{H}_H(\beta) = \langle \Phi | \mathcal{R}(\beta) | \Phi \rangle \times \langle \Phi | e^V \mathcal{R}^{-1}(\beta) U^\dagger \mathcal{R}(\beta) \breve{H} U | \Phi \rangle. \tag{49}$$

Here, the operator $V(\beta)$ results from Eq. (24) by replacing $R(\beta) \to \mathcal{R}(\beta)$. (This has to be kept in mind for the rest of this subsection.)

We insert the identity $1 = \exp(-V)\exp(V)$ three times and use $\exp(V)|\Phi\rangle = |\Phi\rangle$. This yields

$$\mathcal{H}_H(\beta) = \langle \Phi | \mathcal{R}(\beta) | \Phi \rangle \langle \Phi | \widetilde{U}^\dagger \overline{H}\, \overline{U} | \Phi \rangle, \tag{50}$$

where

$$\widetilde{U}^\dagger \equiv e^V \mathcal{R}^{-1}(\beta) U^\dagger \mathcal{R}(\beta) e^{-V}. \tag{51}$$

Because the similarity transformation (28) is presently applied to $\breve{H}$ and not to H, the notation $\overline{\breve{H}}$ should have been used in Eq. (50). For simplicity we continue to use the lighter notation $\overline{H}$. The operators in Eq. (50) all depend on β and therefore do not commute with J_z. This increases the storage demands.

Equation (50) requires us to perform a number of basis transformations followed by taking expectation values of a product consisting of up to three two-body operators. To do this, we insert a resolution of the identity in terms of the reference state and its particle-hole excitations:

$$\mathcal{H}_H(\beta) = \langle \Phi | \mathcal{R}(\beta) | \Phi \rangle \sum_\mu \langle \Phi | \widetilde{U}^\dagger | \mu \rangle \langle \mu | \overline{H}\, \overline{U} | \Phi \rangle. \tag{52}$$

The sum truncates to the finite set of states $|\mu\rangle \in \{|\Phi\rangle, |\Phi_i^a\rangle, |\Phi_{ij}^{ab}\rangle, |\Phi_{ijk}^{abc}\rangle, |\Phi_{ijkl}^{abcd}\rangle\}$ including up to 4p-4h excitations. The norm kernel is dealt with in a similar fashion, i.e.,

$$\begin{aligned}\mathcal{N}_H(\beta) &= \langle \Phi | \mathcal{R}(\beta) | \Phi \rangle \langle \Phi | \widetilde{U}^\dagger \overline{U} | \Phi \rangle \\ &= \langle \Phi | \mathcal{R}(\beta) | \Phi \rangle \sum_{\mu'} \langle \Phi | \widetilde{U}^\dagger | \mu' \rangle \langle \mu' | \overline{U} | \Phi \rangle,\end{aligned} \tag{53}$$

where the sum now truncates to the smaller set $|\mu'\rangle \in \{|\Phi\rangle, |\Phi_i^a\rangle, |\Phi_{ij}^{ab}\rangle\}$ of up to 2p-2h excitations.

5. Algebraic expressions

Let us work out the algebraic expression of the norm and Hamiltonian kernels given in Eqs. (53) and (52), respectively. We focus on

$$\overline{U}|\Phi\rangle = \left(1 + \overline{T}_2 + \tfrac{1}{2}\overline{T}_2^2\right)|\Phi\rangle. \tag{54}$$

Here,

$$\overline{T}_2 = \overline{T}_2^{(0)} + \overline{T}_2^{(1)} + \overline{T}_2^{(2)} \tag{55}$$

is decomposed into zero, one, and two-body operators (as indicated by the subscript) and the normal-ordered components are

$$\overline{T}_2^{(0)} = \frac{1}{2}\sum_{ij} \bar{t}_{ij}^{ij}, \tag{56a}$$

$$\overline{T}_2^{(1)} = \sum_{ipq} \bar{t}_{iq}^{ip} \{c_p^\dagger c_q\} \equiv \sum_{pq} \tau_q^p \{c_p^\dagger c_q\}, \tag{56b}$$

$$\overline{T}_2^{(2)} = \frac{1}{4}\sum_{pqrs} \bar{t}_{rs}^{pq} \{c_p^\dagger c_q^\dagger c_s c_r\}. \tag{56c}$$

We introduced $\tau_q^p \equiv \sum_i \bar{t}_{iq}^{ip}$ and $\{\cdots\}$ denotes the normal ordering. By virtue of Thouless's theorem, the amplitudes of the

similarity-transformed cluster operators can be obtained via a transformation of the single-particle basis; see Appendix A for details.

Only the excitation part of the operators (55) matters in Eq. (54). Thus, we limit ourselves to the excitation part of $\overline{U}$ and rewrite Eq. (54) as

$$\overline{U}|\Phi\rangle = (\overline{U}^{(0)} + \overline{U}^{(1)} + \overline{U}^{(2)} + \overline{U}^{(3)} + \overline{U}^{(4)})|\Phi\rangle. \quad (57)$$

Again, we used subscripts (k) to denote a k-body operator. The amplitudes of the excitation operators

$$\overline{U}^{(k)} = \sum_{i_1\cdots i_k}\sum_{a_1\cdots a_k} \overline{u}^{a_1\cdots a_k}_{i_1\cdots i_k} c^\dagger_{a_1}\cdots c^\dagger_{a_k} c_{i_k}\cdots c_{i_1} \quad (58)$$

can be expressed in terms of those introduced in Eq. (56). The corresponding algebraic expressions for

$$\overline{U}^{(0)} = \langle\Phi|\overline{U}|\Phi\rangle, \quad (59a)$$

$$\overline{u}^a_i = \langle\Phi^a_i|\overline{U}|\Phi\rangle, \quad (59b)$$

$$\overline{u}^{ab}_{ij} = \langle\Phi^{ab}_{ij}|\overline{U}|\Phi\rangle \quad (59c)$$

$$\overline{u}^{abc}_{ijk} = \langle\Phi^{abc}_{ijk}|\overline{U}|\Phi\rangle, \quad (59d)$$

$$\overline{u}^{abcd}_{ijkl} = \langle\Phi^{abcd}_{ijkl}|\overline{U}|\Phi\rangle \quad (59e)$$

are presented in Appendix B 1. The matrix elements associated with the bra state $\langle\Phi|\widetilde{U}^\dagger$ follow from the above derivation by exchanging particle and hole indices, and by replacing the matrix elements of the similarity-transformed operator $\overline{T}_2$ by those of $\widetilde{T}_2$ defined similarly to Eq. (51). With these matrix elements at hand, the norm kernel (53) can be evaluated.

To evaluate the Hamiltonian kernel (52) we also need the matrix elements

$$\overline{X}^{(0)} \equiv \langle\Phi|\overline{HU}|\Phi\rangle, \quad (60a)$$

$$\overline{x}^a_i \equiv \langle\Phi^a_i|\overline{HU}|\Phi\rangle, \quad (60b)$$

$$\overline{x}^{ab}_{ij} \equiv \langle\Phi^{ab}_{ij}|\overline{HU}|\Phi\rangle, \quad (60c)$$

$$\overline{x}^{abc}_{ijk} \equiv \langle\Phi^{abc}_{ijk}|\overline{HU}|\Phi\rangle, \quad (60d)$$

$$\overline{x}^{abcd}_{ijkl} \equiv \langle\Phi^{abcd}_{ijkl}|\overline{HU}|\Phi\rangle \quad (60e)$$

in terms of those of the normal-order pieces of $\overline{H}$ and $\overline{U}$. These expressions are presented in Appendix B 2.

Using these ingredients, the kernels can finally be computed as

$$\frac{\mathcal{H}_H(\beta)}{\langle\Phi|\mathcal{R}(\beta)|\Phi\rangle} = \widetilde{U}^{\dagger(0)}\overline{X}^{(0)} + \sum_{ai}\widetilde{u}^i_a\overline{x}^a_i + \frac{1}{4}\sum_{abij}\widetilde{u}^{ij}_{ab}\overline{x}^{ab}_{ij} + \frac{1}{36}\sum_{abcijk}\widetilde{u}^{ijk}_{abc}\overline{x}^{abc}_{ijk} + \frac{1}{576}\sum_{abcdijkl}\widetilde{u}^{ijkl}_{abcd}\overline{x}^{abcd}_{ijkl}, \quad (61a)$$

$$\frac{\mathcal{N}_H(\beta)}{\langle\Phi|\mathcal{R}(\beta)|\Phi\rangle} = \widetilde{U}^{\dagger(0)}\overline{U}^{(0)} + \sum_{ai}\widetilde{u}^i_a\overline{u}^a_i + \frac{1}{4}\sum_{abij}\widetilde{u}^{ij}_{ab}\overline{u}^{ab}_{ij} + \frac{1}{36}\sum_{abcijk}\widetilde{u}^{ijk}_{abc}\overline{u}^{abc}_{ijk} + \frac{1}{576}\sum_{abcdijkl}\widetilde{u}^{ijkl}_{abcd}\overline{u}^{abcd}_{ijkl}. \quad (61b)$$

Naively estimated, the inclusion of T_2^2 in the bra and ket states of the Hamiltonian kernel comes at a considerable cost of $n_u^6 n_o^4$ computational cycles, with n_u the number of unoccupied and n_o the number of occupied states, respectively. However, $\overline{U}^{(4)}$ is a product of two disconnected terms and this reduces the cost to $n_u^5 n_o^4$ because intermediates can be introduced. In Eq. (61a), for example, we first compute a three-body intermediate by contracting $\overline{T}_2^{(2)}$ with $\overline{H}$ and this is then followed by a contraction with the second $\overline{T}_2^{(2)}$. We note that the SLD and the disentangled approaches used in this work scale as $n_u^4 n_o^2$ (which is the familiar CCSD scaling), but they require significant larger computational resources than the unprojected CCSD solution because J_z is not a good quantum number in the projection.

V. COLLECTIVE HAMILTONIAN AND EFFECTIVE THEORY

A. Collective Hamiltonian

The expressions derived so far allow us to compute the collective Hamiltonian [78,90–92]. Let $\Omega \equiv (\theta, \phi)$ consist of a polar angle and azimuth, and let

$$|\Omega\rangle \equiv e^{-i\phi J_z} e^{-i\theta J_y}|\Psi\rangle \quad (62)$$

be a rotation of the state $|\Psi\rangle$. Thus, in the state $|\Omega\rangle$ the symmetry axis of the nucleus points into the direction of the radial unit vector $\mathbf{e}_r(\theta, \phi)$. The matrix elements

$$\mathcal{H}(\Omega', \Omega) \equiv \langle\Omega'|H|\Omega\rangle, \quad \mathcal{N}(\Omega', \Omega) \equiv \langle\Omega'|\Omega\rangle \quad (63)$$

are related to the kernels (39) via

$$\mathcal{H}(\Omega', \Omega) = \mathcal{H}_H(\beta), \quad \mathcal{N}(\Omega', \Omega) = \mathcal{N}_H(\beta), \quad (64)$$

where $\cos\beta = \mathbf{e}_r(\theta, \phi)\cdot\mathbf{e}_r(\theta', \phi')$. The collective Hamiltonian then becomes

$$H_{\text{coll}}(\Omega', \Omega) = [\mathcal{N}^{-\frac{1}{2}}\mathcal{H}\mathcal{N}^{-\frac{1}{2}}](\Omega', \Omega). \quad (65)$$

To compute the matrix elements (64) we distribute a few tens of angles Ω evenly over the sphere, following Ref. [93]. The diagonalization of H_{coll} then yields the low-lying collective spectrum, and the corresponding collective state can be used to compute other observables or transition matrix elements of interest. An alternative approach to the collective Hamiltonian is via effective field theory (EFT).

B. Effective theory

At lowest energies, the only degree of freedom for an axially symmetric even-even nucleus is the orientation $\mathbf{e}_r(\theta,\phi)$ of its symmetry axis [32,35], where (θ,ϕ) define the polar and azimuth angles. Following arguments from spontaneous [94] and emergent symmetry breaking [91,92,95] the effective Hamiltonian can only contain the angular derivative

$$\boldsymbol{\nabla}_\Omega \equiv \mathbf{e}_\theta \frac{\partial}{\partial\theta} + \mathbf{e}_\phi \frac{1}{\sin\theta}\frac{\partial}{\partial\phi}. \tag{66}$$

Here, $\mathbf{e}_\theta$ and $\mathbf{e}_\phi$ denote the polar and azimuth unit vectors that, together with the radial unit vector $\mathbf{e}_r$, form the body-fixed coordinate system. The leading-order effective Hamiltonian is [32]

$$H_{\rm EFT} = E^{(0)} + a(-i\boldsymbol{\nabla}_\Omega)^2. \tag{67}$$

Here, the low-energy coefficients $E^{(0)}$ and a are the ground-state energy and the rotational constant, respectively. Thus, the constraints from emergent symmetry breaking ensure that the effective Hamiltonian (67) can be matched to the collective Hamiltonian (65) by adjusting $E^{(0)}$ and a. The low-energy coefficient $E^{(0)}$ contains short-range physics, and one needs size-extensive methods to compute it. In contrast, the rotational constant a is the inverse moment of inertia and depends on the nuclear shape and—for heavy nuclei—also on the degree of superfluidity. Thus, computing a does not require high-resolution methods. As we will see below, mean field methods (which are quite inaccurate regarding $E^{(0)}$) yield reasonable values for a in the nuclei we compute.

Introducing the angular momentum $\hat{J} = \mathbf{e}_r \times (-i\boldsymbol{\nabla}_\Omega)$ allows us to rewrite the effective Hamiltonian (67) as

$$H_{\rm EFT} = E^{(0)} + a\hat{J}^2. \tag{68}$$

This is the Hamiltonian of the rigid-rotor model, and its spectrum is

$$E^{(J)} = E^{(0)} + aJ(J+1). \tag{69}$$

Taking the expectation value of the effective Hamiltonian (68) in the unprojected wave function yields

$$E = E^{(0)} + a\langle J^2\rangle. \tag{70}$$

Thus, the ground-state energy gain from projection is

$$\delta E \equiv E^{(0)} - E = -a\langle J^2\rangle, \tag{71}$$

delivering the result of Peierls and Yoccoz [96].

To check the consistency of these arguments we return to Eqs. (69) and (71) and find

$$E^{(J)} - E^{(0)} = -\delta E \frac{J(J+1)}{\langle J^2\rangle} \tag{72}$$

for the excitation energy of the state with spin J. To estimate the ground-state energy gain from projection we use

$$\delta E = (E^{(0)} - E^{(2)})\frac{\langle J^2\rangle}{6}, \tag{73}$$

where $E^{(0)}$ and $E^{(2)}$ result from, e.g., angular momentum projection. Taking instead the energy difference $E^{(0)} - E^{(2)}$ from experimental data (i.e., 3 MeV in ^{8}Be, 0.6 MeV in the island of inversion), one immediately obtains an estimate for the energy gain from symmetry projection by employing the expectation value $\langle J^2\rangle$ of the symmetry-unrestricted state. The energy gain from projection is much smaller than the energy from dynamical correlations, which allows us to employ approximations that lack size extensivity. It is also clear from Eq. (73) that the gain from symmetry restoration is proportional to the expectation value $\langle J^2\rangle$ of the unprojected state. Thus, including more correlations in that state is expected to reduce the value $\langle J^2\rangle$ and the energy gain from projection.

The approach via effective field theory also enables us to estimate uncertainties. The first step involves the identification of a breakdown scale. For simplicity we use here a breakdown spin $J_{\rm b}$ where new physics enters; the corresponding breakdown energy, relative to the ground-state energy $E^{(0)}$, is then $\Lambda_{\rm b} = aJ_{\rm b}(J_{\rm b}+1)$. The subleading correction to the Hamiltonian (68) is the term $b(\hat{J}^2)^2$, which adds the contribution $b[J(J+1)]^2$ to the spectrum (69); see, e.g., Ref. [32]. At the breakdown scale, the subleading contribution becomes significant, and this allows us to estimate the unknown coefficient b. A simple estimate can be obtained by assuming that the leading and subleading contributions are approximately equal in size at the breakdown scale; this yields $b \approx a/[J_{\rm b}(J_{\rm b}+1)]$. A more realistic assumption is that the subleading term is of the same size as the leading-order level spacing $E^{(J_{\rm b}+1)} - E^{(J_{\rm b}-1)} = 2a(J_{\rm b}+1)$ at the breakdown scale; this yields the estimate

$$b \approx \frac{2a}{J_{\rm b}^2(J_{\rm b}+1)}. \tag{74}$$

With this assumption about the breakdown scale, the uncertainty at spin $J \lesssim J_{\rm b}$ is

$$\Delta E^{(J)} \approx 2a\frac{[J(J+1)]^2}{J_{\rm b}^2(J_{\rm b}+1)}. \tag{75}$$

Using more information than merely the breakdown scale (or making more assumptions), would allow us to quantify uncertainties [97–99]. Here, we will contend ourselves with the estimate (75). Long sequences of data would also allow us to empirically determine the breakdown scale, e.g., via Lepage plots [36].

The rotational constant a is inverse proportional to the moment of inertia which—for a liquid drop—is proportional to $A^{5/3}$ where A is the mass number. Taken together with the empirical relation $\langle J^2\rangle \sim A^{3/2}$ from mean-field calculations [69] then implies that the energy gain from symmetry projection is small and decreases with increasing mass number. Long-wavelength physics dominates angular momentum projection. We can also see this in an equation-of-motion approach where the (non-normalized) excited $J^\pi = 2^+$ state is

$$|2^+\rangle = Q_{20}^{(p)}|0^+\rangle. \tag{76}$$

Here the charge quadrupole operator $Q_{20}^{(p)}$ is defined as in Eq. (4) but the sum is over protons. This long-range operator is insensitive to short-range physics. The equation-of-motion approach to excited states then yields

$$\left[H, Q_{20}^{(p)}\right]|0^+\rangle = (E^{(2)} - E^{(0)})Q_{20}^{(p)}|0^+\rangle. \tag{77}$$

Employing the effective Hamiltonian (68) in Eq. (77) yields $E^{(2)} - E^{(0)} = 6a$ because $Q_{20}^{(p)}$ is a spherical tensor of rank 2. Thus, rotational excitation energies are low-resolution observables and can be computed with low-resolution methods.

The quadrupole operator connects harmonic oscillator shells that differ by two units of $\hbar\omega$. Thus, the equation-of-motion approach also shows that microscopic computations of the states with angular momentum $J = 2, 4, 6, \ldots$ via symmetry projection requires model spaces that exceed the Fermi surface by J shells.

A future goal consists of computing quadrupole moments of projected states and transition matrix elements between projected states. For now, we characterize collectivity via a phenomenological approach. The quadrupole deformation parameter for a charged liquid drop is [100]

$$\beta_2 \equiv \frac{\sqrt{5\pi}\langle Q_{20}^{(p)}\rangle}{3ZR_0^2}, \tag{78}$$

where $R_0 = 1.2A^{1/3}$ fm is the empirical charge radius. The optimized next-to-next-to leading order ($\mathrm{NNLO_{opt}}$) potential yields too small radii for all but the lightest nuclei [101–104]. To compute the quadrupole deformation parameter we therefor replace R_0^2 by the charge radius squared (R_{ch}^2). Computing expectation values in the unprojected ground state, the deformation parameter then becomes

$$\beta_2 \equiv \frac{\sqrt{5\pi}\langle Q_{20}^{(p)}\rangle}{3ZR_{ch}^2}. \tag{79}$$

Superfluid systems that break particle number can similarly be addressed in an effective theory. One then replaces the orientation of the symmetry axis by the gauge angle and $a\hat{J}^2$ by the pairing rotational term $b(\hat{A} - \langle\hat{A}\rangle)^2$ where b is a low-energy coefficient and $\hat{A}$ the number operator. The energy gain (71) from particle-number projection is then related to the particle-number variation of the unprojected state. For an estimate in medium-mass nuclei we note that $b \approx 0.1$ MeV in tin isotopes [105] and that $\langle(A - \langle A\rangle)^2\rangle \approx 16$–$36$ in nickel isotopes [19]. Thus, particle-number projections do also not seem to require size extensive methods.

VI. RESULTS FOR ^{8}Be, ^{20}Ne, AND ^{34}Mg

We compute the nuclei ^{8}Be, ^{20}Ne, and ^{34}Mg using the nucleon-nucleon interaction $\mathrm{NNLO_{opt}}$ [106]. For ^{8}Be, we benchmark with the no-core shell model (NCSM) [27,28] and for ^{20}Ne with the symmetry-adapted NCSM [31]. These benchmarks are close to experimental data, and the accuracy of the $\mathrm{NNLO_{opt}}$ potential makes it interesting to compute the structure of the neutron-rich nucleus ^{34}Mg.

The Hamiltonian (7) is the sum of the intrinsic kinetic energy (to decouple the center-of-mass mode [107–109]) and the two-body potential. We use a single particle basis that consists of the eigenstates $\{|p\rangle \equiv |nljj_zt_z\rangle\}$ with energy $(2n + l)\hbar\omega$ of the spherical harmonic oscillator (omitting the zero-point energy). States with an energy up to and including $N_{\max}\hbar\omega$ are in the basis.

For the construction of the reference state, shells are filled according to the nuclear shell model [110]. The partially occupied subshell at the Fermi surface is filled by occupying Kramer-degenerate pairs of states with increasing values $|j_z| = 1/2, 3/2, \ldots$ of the angular-momentum projection. This leads to prolate deformation. The various reference states we used are described in Sec. III.

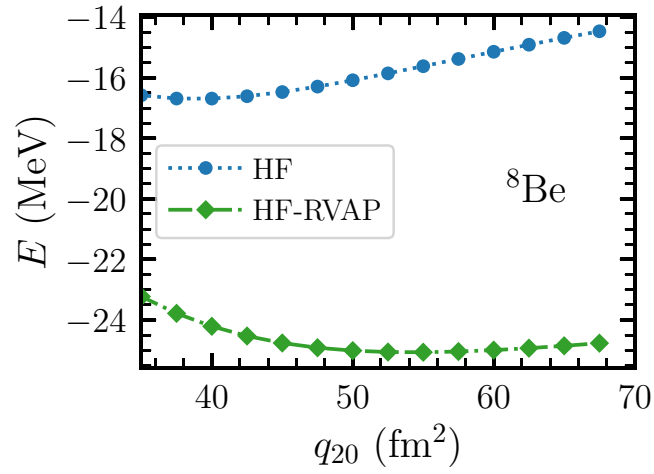

FIG. 1. Energies of ^{8}Be from symmetry-unrestricted Hartree-Fock (blue circles) and HF-RVAP (green diamonds) as a function of the mass quadrupole moment q_{20}. Calculations are performed with $\hbar\omega = 24$ MeV.

Figure 1 shows the energy of the reference states from Hartree-Fock and from HF-RVAP for ^{8}Be as a function of quadrupole moment. The projection shifts the minimum towards a larger value of the quadrupole moment.

We found that the Hermitian SLD and SQD approximations are insensitive to the choice of the reference state presumably because we treat the singles excitations e^{T_1} exactly. As we will see below these approaches also meet benchmarks from NCSM calculations [27,31]. The disentangled approach yields somewhat too compressed spectra, particularly for the CCSD approximation. The CCSD spectra exhibit a small spread with respect to the reference state. The level spacing increases as we go from Hartree Fock to HF-RVAP to HF-VAP, and the CCSD results also depend mildly on the chosen oscillator spacing. We attribute the compressed spectra to the simple energy expression (19), which is not a bivariational energy functional. In contrast, results for the CCD approximation are somewhat more accurate when compared to the benchmarks. This, however, limits us to the Hartree-Fock basis where singles excitations $[\exp(T_1)]$ are small.

A. Operator kernels

Figure 2 shows the norm and Hamiltonian kernels in ^{20}Ne and ^{34}Mg, respectively, as a function of rotation angle β for the disentangled formalism and compares them to Hartree-Fock kernels. Here we employed the Hartree-Fock basis and a model space with $N_{\max} = 7$ and $\hbar\omega = 24$ MeV. At $\beta = 0$ the Hamiltonian kernels yield the energies of the unprojected Hartree-Fock and CCD states. The Hartree-Fock kernels exhibit the $\mathcal{R}$ parity and are symmetric upon reflection at $\beta =$

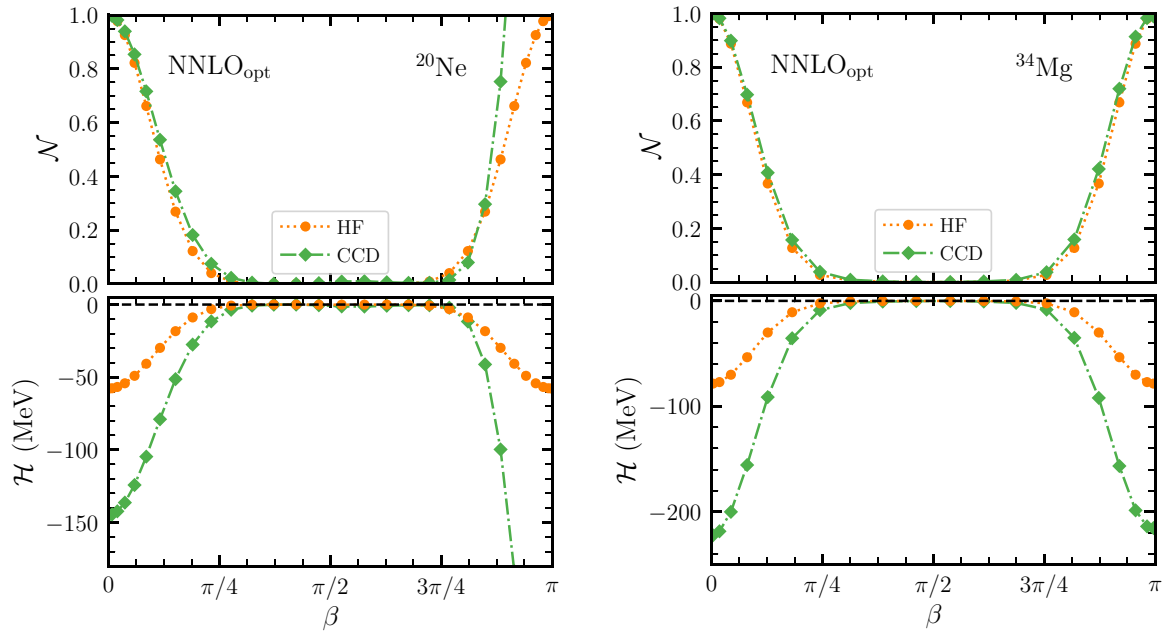

FIG. 2. Kernels for ^{20}Ne (left panels) and ^{34}Mg (right panels) as a function of the rotation angle. The norm kernels (top panels) and Hamiltonian kernels (bottom panels) are shown for Hartree-Fock (orange circles) and CCD (green diamonds) calculations. We employed the Hartree-Fock basis and a model space with $N_{\rm max} = 7$ and $\hbar\omega = 24$ MeV.

$\pi/2$. The disentangled formalism approximates the rotation operator and does not keep the $\mathcal{R}$ parity. This is clearly seen for the case of ^{20}Ne while less so for ^{34}Mg. To avoid problems we assume $\mathcal{R}$ parity and limit the domain of integration in Eq. (20) to $[0, \pi/2]$. This ensures that odd angular momenta are excluded from the ground-state rotational band.

In the absence of symmetry breaking, the kernels are constant and do not depend on β. Therefore, one expects that operator kernels flatten out at higher truncation levels [58]. The upper panels of Fig. 2 show that this is indeed the case. An alternative view is as follows: The curvature of the norm kernel at $\beta = 0$ is proportional to the expectation value $\langle \hat{J}^2 \rangle$ of the unprojected state, and this value should decrease with increasing sophistication of the employed many-body wave function. Figure 2 confirms this.

How do the truncations in the disentangled formalism impact the projection? To address this question we computed the expectation value of $\hat{J}^2$ in the projected states. We found that the difference to $J(J+1)$ is less than 0.4 for $J = 0$, less than 4% for $J = 2$, and less than 2% for $J = 4$. Deviations where largest for ^{20}Ne and smallest for ^{34}Mg. We speculate that is because the ^{34}Mg spectrum is closest to a rigid rotor.

B. Spectra of ^{8}Be and ^{20}Ne

Figure 3 displays the ground-state rotational band of ^{8}Be computed with the CCD (left panel), the SLD (middle panel), and the SQD approximations (right panel). With CCD the excitation energy of the $J^\pi = 2^+$ state is converged for $N_{\rm max} = 7$ and practically independent of $\hbar\omega$. The first 4^+ energy still exhibits some dependence on the basis. The convergence pattern is somewhat different for the SLD and SQD approximations. Here, the the 2^+ energy starts to converge with $N_{\rm max} = 3$ and the 4^+ energy at $N_{\rm max} = 5$. This is consistent with the discussions below Eqs. (76) and (77), because the Fermi surface of ^{8}Be is in the $N_{\rm max} = 1$ shell.

In the disentangled CCD approximation, the projected energies are lower than the NCSM benchmarks [27], i.e., the excitation energy of the $J^\pi = 2^+$ state is 1 MeV too low whereas the 4^+ excitation energy differs by about 2 MeV. In the SLD approximation, the 2^+ energy is close to the NCSM

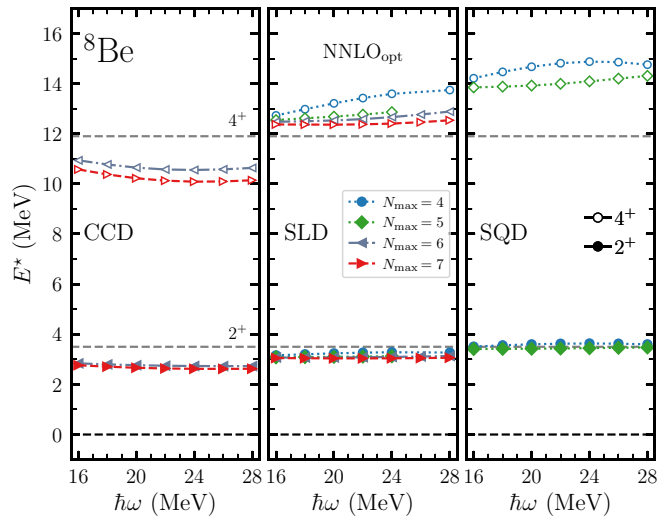

FIG. 3. Projected coupled-cluster excitation energies for ^{8}Be as a function of oscillator frequency obtained from CCD (left panel), SLD (middle panel), and SQD approximations (right panel). Model spaces are labeled by $N_{\rm max}$. Horizontal dashed grey lines show NCSM results.

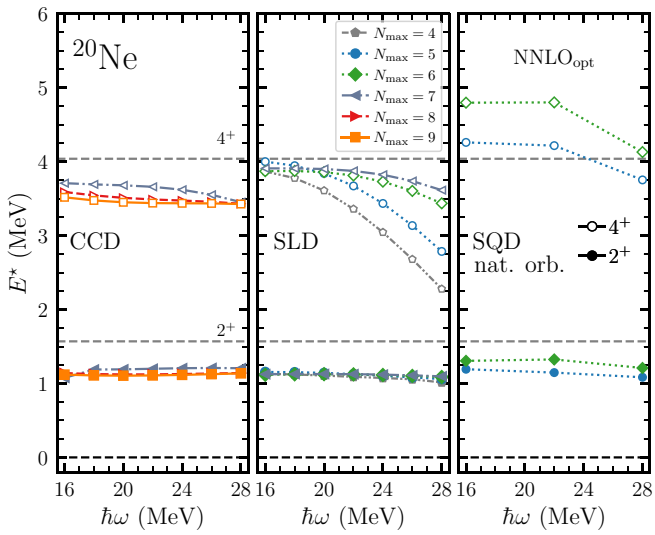

FIG. 4. Projected coupled-cluster excitation energies for ^{20}Ne as a function of oscillator frequency obtained from CCD (left panel), SLD (middle panel), and SQD approximations (right panel). Model spaces are labeled by N_{max}. Horizontal dashed grey lines show NCSM results.

result whereas the converged 4^+ energy is about 0.5 MeV (4%) too high. Finally, the 2^+ energy from SQD agrees with the benchmark while the the 4^+ energy is too high.

For ^{20}Ne we compare with benchmarks from the symmetry adapted NCSM [31] and show results in Fig. 4. For the SLD and SQD approximations the energies of the $J^\pi = 2^+$ and 4^+ states start to converge at $N_{max} = 4$ and $N_{max} = 4$ and $N_{max} = 6$, respectively, because the Fermi surface is in the $N_{max} = 2$ shell. The SLD results display an optimal harmonic oscillator frequency around 16 MeV, and the spectrum is slightly compressed compared to NCSM. For CCD we employed up to ten major harmonic oscillator shells which is large enough for convergence. As can be seen the spectrum is too compressed and resemble too much that of a rigid rotor. We also employed the CCSD approximation for the largest model space and found the 2^+ energy at 1 MeV and the 4^+ energy at ≈3 MeV. Computing rotational spectra via projection requires much smaller model spaces than required for ground-state energies. This is consistent with our discussion in Sec.. V B and Ref. [53]. The symmetry restoration involves a nonperturbative mixing of states close to the Fermi surface such that a comparably small number of harmonic oscillator shells is sufficient to obtain converged results. As observed when going from ^{8}Be to ^{20}Ne, the model space requirements increase with increasing mass number because of the reference state.

Let us match the EFT to our results. The leading-order EFT spectrum (69) depends on two low-energy constants. We use the ground-state energy gained through projection, δE, and the expectation value $\langle J^2 \rangle$ of the unprojected state as input to the EFT and determine the excitation spectrum via Eq. (72). Uncertainties are estimated by Eq. (75). For ^{8}Be the breakdown energy $\Lambda_b \approx 20$ MeV is set by the energy of α particle excitations; the corresponding breakdown spin is $J_b \approx 5$. Figure 5 shows the EFT spectra (red error bars) based on the input from projected Hartree-Fock and projected coupled-cluster results in Table I using three different single-particle bases. Also shown are NCSM benchmarks. About two-thirds of the EFT results agree with the energies of the Hartree-Fock and coupled-cluster calculations. For the $J^\pi = 2^+$ states the energy ranges from the EFT are systematically higher than the projected energies and the NCSM result. The EFT ranges for the energy of the 4^+ state agree with the microscopic computations.

The projected Hartree-Fock results are close to the NSCM benchmarks. This is in contrast to the ground-state energies shown at the bottom of the plot (in units of MeV). While the total binding energy requires dynamical correlations, the low-lying rotational excitations are dominated by static correlations and well captured through the symmetry restoration; see also Ref. [53]. The coupled-cluster computations in-

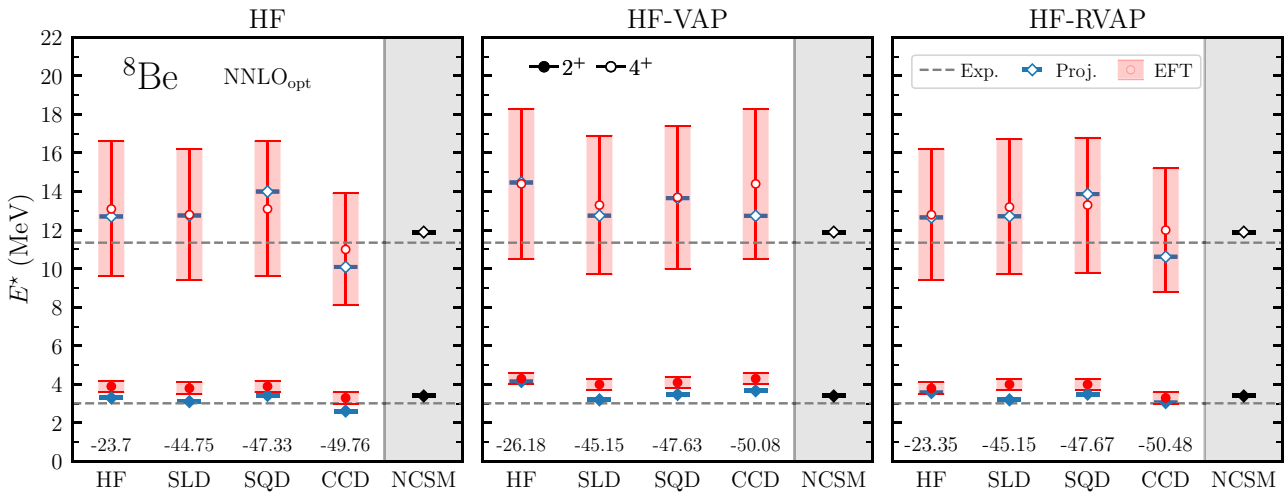

FIG. 5. Low-lying excitation energies of ^{8}Be from projected Hartree-Fock (HF), projected coupled-cluster (SLD, SQD, and CCD) computations, and leading-order EFT using HF, HF-VAP, and HF-RVAP reference states (from left to right). Also shown are NSCM benchmarks and experiment (dashed lines). The numbers at the bottom of the plot are projected ground-state energies (in MeV).

TABLE I. Results for ^{8}Be. Here, E and $\langle J^2\rangle$ are the unprojected ground-state energy and angular momentum expectation values, respectively, δE the gain of the ground-state energy from projection, and $E^{(J)}$ is the energy of the excited state with spin J. All energies are in MeV. For the projection we employed a model-space with $N_{\max} = 5$ and $\hbar\omega = 22$ MeV for HF, HF-VAP, HF-RVAP, SLD, and SQD, while $N_{\max} = 7$ and $\hbar\omega = 24$ MeV for CCD. The SLD and SQD unprojected expectation values are obtained using the $\beta = 0$ kernels. The CCD unprojected results were obtained using the linear-response approach. The EFT results are obtained by using δE and $\langle J^2\rangle$ as input; uncertainties are based on the assumption that the breakdown scale is at about 20 MeV of excitation energy. The NCSM results [27] are $E^{(2)} - E^{(0)} = 3.5$ MeV and $E^{(4)} - E^{(0)} = 11.9$ MeV.

	Unprojected		Projected				EFT	
^{8}Be	E	$\langle J^2\rangle$	δE	$E^{(0)} = E + \delta E$	$E^{(2)} - E^{(0)}$	$E^{(4)} - E^{(0)}$	$E^{(2)} - E^{(0)}$	$E^{(4)} - E^{(0)}$
HF	−16.304	11.270	−7.399	−23.70	3.33	12.71	3.9 ± 0.3	13.1 ± 3.5
SLD	−39.829	7.724	−4.923	−44.75	3.11	12.76	3.8 ± 0.3	12.8 ± 3.4
SQD	−43.179	6.311	−4.146	−47.33	3.43	14.00	3.9 ± 0.3	13.1 ± 3.5
CCD	−45.907	6.998	−3.852	−49.76	2.62	10.09	3.3 ± 0.3	11.0 ± 2.9
HF-VAP	−13.535	17.502	−12.640	−26.18	4.15	14.47	4.3 ± 0.3	14.4 ± 3.9
SLD	−39.564	8.379	−5.588	−45.15	3.20	12.75	4.0 ± 0.3	13.3 ± 3.6
SQD	−42.812	7.033	−4.819	−47.63	3.48	13.66	4.1 ± 0.3	13.7 ± 3.7
CCD	−41.961	11.243	−8.123	−50.08	3.67	12.74	4.3 ± 0.3	14.4 ± 3.9
HF-RVAP	−13.535	15.335	−9.815	−23.35	3.58	12.66	3.8 ± 0.3	12.8 ± 3.4
SLD	−39.604	8.418	−5.547	−45.15	3.20	12.72	4.0 ± 0.3	13.2 ± 3.5
SQD	−43.112	6.844	−4.559	−47.67	3.50	13.87	4.0 ± 0.3	13.3 ± 3.5
CCD	−44.979	9.165	−5.498	−50.48	3.06	10.62	3.3 ± 0.3	12.0 ± 3.2

clude dynamical correlations and achieve lower ground-state energies. Clearly, those correlations contribute little to the rotational spectrum.

Table I summarizes our results for ^{8}Be. We note that $\langle J^2\rangle$ of the unprojected state and energy gained from projection, δE, decrease a lot from Hartree-Fock to coupled-cluster computations because the latter include much more dynamical correlations. We also note that the projected HF results for the spectrum are more accurate than the projected CCD results in the Hartree-Fock basis.

As can be seen in Table I the Hermitian SLD and SQD results depend only weakly on the choice of reference due to the exact treatment of $\exp(T_1)$ in the projection. In contrast the CCD results exhibit a considerable dependence on the reference states. The CCD calculations in the HF basis are probably most consistent because the unprojected T_1 amplitudes are small. One would expect that projected CCSD would alleviate the dependence on the reference state, and calculations show that this is indeed the case. However, the resulting spectra are more compressed and less accurate than CCD. This is presumably due to the simple parametrization of the bra state. For these reasons, and limited computational resources, we limit our calculations for ^{20}Ne and ^{34}Mg in the CCD approximation to the HF reference. Future work will employ the CCSD bivariational functional in the projection.

For ^{20}Ne we show results computed with the Hartree-Fock basis in Fig. 6 (here the results shown in Table II were used as input for the EFT predictions). The EFT uncertainties are based on a breakdown angular momentum $J_b \approx 5$ which corresponds to a breakdown energy of about 7 MeV. At this energy, positive-parity states appear that are not part of the ground-state rotational band. As for ^{8}Be, the EFT ranges are above the computed energies for $J^\pi = 2^+$ but agree for the 4^+ levels.

Table II summarizes our results for ^{20}Ne in the Hartree-Fock basis using a model space with $N_{\max} = 7$ and with the oscillator frequency $\hbar\omega = 20$ MeV. We see in particular that the charge radius R_{ch} is virtually unchanged by the projection. This validates several calculations of charge radii [20,111].

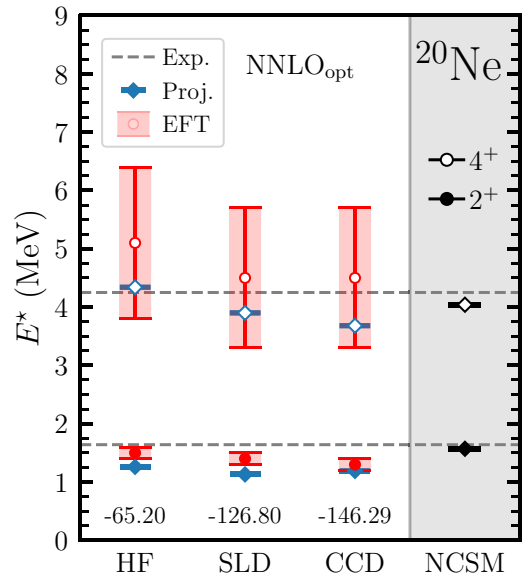

FIG. 6. Excitation energies of ^{20}Ne from projected Hartree-Fock and projected coupled-cluster (SLD and CCD) computations compared to EFT results, the benchmark from the symmetry-adapted NCSM, and experiment (dashed lines). The numbers at the bottom of the plot are projected ground-state energies (in MeV). For the projection we employed a Hartree-Fock basis in a model space with $N_{\max} = 7$ and with oscillator frequency $\hbar\omega = 20$ MeV.

TABLE II. Results for ^{20}Ne. Here, E and $\langle J^2\rangle$ are the unprojected ground-state energy and angular momentum expectation values, respectively, R_{ch} is the charge radius, δE the gain of the ground-state energy from projection, and $E^{(J)}$ is the energy of the excited state with spin-parity J. All energies are in MeV. For the projection we employed the Hartree-Fock basis in a model space with $N_{\max} = 7$ and with the oscillator frequency $\hbar\omega = 20$ MeV. The SLD unprojected expectation values were obtained using the $\beta = 0$ kernels. The CCD unprojected expectation value for R_{ch} were obtained using the $\beta = 0$ kernel while for $\langle J^2\rangle$ we used the linear response approach. The EFT results are obtained by using δE and $\langle J^2\rangle$ as input; uncertainties are based on the assumption that the breakdown spin is $J_b \approx 5$. The NCSM benchmarks are $E^{(2)} - E^{(0)} = 1.64$ MeV and $E^{(4)} - E^{(0)} = 4.25$ MeV [31]. The calculated charge radii are smaller than the experimental charge radius, $R_{ch} = 3.0055(21)$ fm [112].

	Unprojected			Projected					EFT	
^{20}Ne	E	$\langle J^2\rangle$	R_{ch} (fm)	δE	$E^{(0)} = E + \delta E$	R_{ch} (fm)	$E^{(2)} - E^{(0)}$	$E^{(4)} - E^{(0)}$	$E^{(2)} - E^{(0)}$	$E^{(4)} - E^{(0)}$
HF	−59.442	22.778	2.623	−5.760	−65.202	2.619	1.26	4.34	1.5 ± 0.1	5.1 ± 1.3
SLD	−122.467	19.059	2.601	−4.332	−126.799	2.598	1.13	3.90	1.4 ± 0.1	4.5 ± 1.2
CCD	−142.666	16.128	2.621	−3.627	−146.293	2.620	1.19	3.68	1.3 ± 0.1	4.5 ± 1.2

We also note that the projected HF results are close to the NCSM benchmark.

C. ^{34}Mg

Neutron-rich magnesium isotopes have long been in the focus of experiment [113–116] and theory [117–119], because they are located in the "island of inversion," where deformed ground states emerge within the shell-model from the presence of intruder orbits [120]. The experiments of Refs. [121–124] observed a ground-state rotational band in ^{34}Mg. This provides us with an opportunity to test our projection methods using the chiral interaction NNLO$_{\rm opt}$ (which is fairly accurate for ^{8}Be and ^{20}Ne).

To facilitate the convergence with respect to the size of the underlying spherical harmonic oscillator basis, we also use natural orbitals for SLD approach. Those are computed from a one-body density matrix following Refs. [85,86,125] in a large basis with $N_{\max} = 12$. We truncate the set of natural orbitals selected based on their large occupations following the procedure described in Ref. [86]. The CCD and SLD results for the low-lying spectrum of ^{34}Mg is shown in Fig. 7 for different $N_{\max}$ and oscillator frequencies in the range $\hbar\omega = 16, \ldots, 28$ MeV. The SQD results would begin to converge at $N_{\max} = 7$ which is computationally too expensive for this nucleus. As can be seen the SLD results are close to data while the spectrum obtained with CCD is too compressed. We also here employed the CCSD approximation in the largest model-space and obtained an even more compressed spectrum with the 2^+ energy at 0.4 MeV and the 4^+ energy at ≈1.3 MeV.

Figure 8 shows the EFT predictions for the low-lying spectrum of ^{34}Mg obtained from projected calculations using Hartree Fock, SLD, and CCD (taken from Table III). The EFT results include uncertainty estimates that are based on

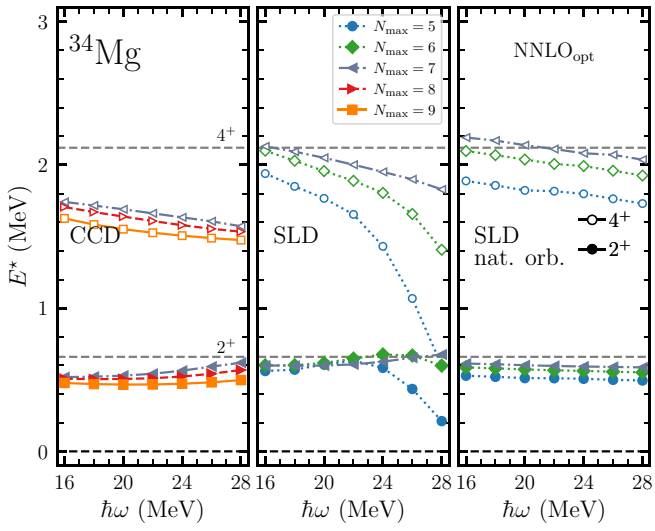

FIG. 7. Projected coupled-cluster excitation energies for ^{34}Mg as a function of oscillator frequency obtained from CCD (left panel), SLD (middle panel), and SLD approximations with natural orbitals (right panel). Model spaces are labeled by $N_{\max}$. Horizontal dashed grey lines show experimental data.

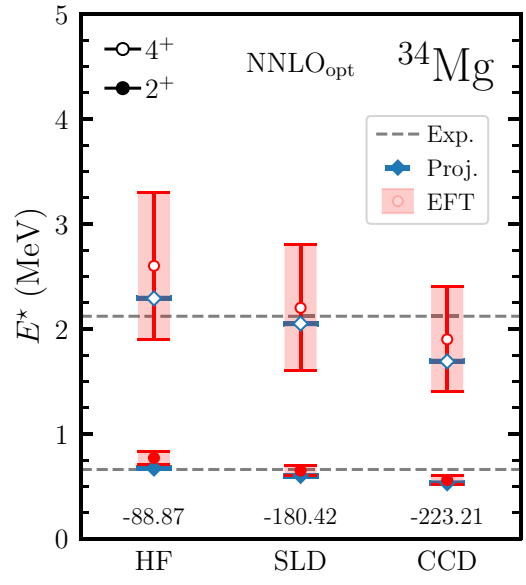

FIG. 8. Excitation energies of ^{34}Mg from projected Hartree-Fock and projected coupled-cluster (SLD and CCD) computations compared to EFT results and experiment (dashed lines), using the results shown in Table III. The numbers at the bottom of the plot are projected ground-state energies (in MeV).

TABLE III. Results for ^{34}Mg. Here, E and $\langle J^2 \rangle$ are the unprojected ground-state energy and angular momentum expectation values, respectively, R_p^2 is the point-proton radius squared (including spin-orbit contributions), δE the gain of the ground-state energy from projection, and $E^{(J)}$ is the energy of the excited state with spin J. All energies are in MeV. For the projection we employed a model space with $N_{\max} = 7$ and with the oscillator frequency $\hbar\omega = 20$ MeV. The SLD unprojected expectation values for were obtained using the $\beta = 0$ kernels. The CCD unprojected expectation value for $\langle R_p^2 \rangle$ were obtained using the $\beta = 0$ kernel while for $\langle J^2 \rangle$ we used the linear response approach. The EFT results are obtained by using δE and $\langle J^2 \rangle$ as input; uncertainties are based on the assumption that the breakdown scale is at about 3.2 MeV, i.e., the breakdown spin is $J_b = 5$.

	Unprojected			Projected					EFT	
^{34}Mg	E	$\langle J^2 \rangle$	R_{ch} (fm)	δE	$E^{(0)} = E + \delta E$	R_{ch} (fm)	$E^{(2)} - E^{(0)}$	$E^{(4)} - E^{(0)}$	$E^{(2)} - E^{(0)}$	$E^{(4)} - E^{(0)}$
HF	−85.687	24.740	2.727	−3.184	−88.87	2.724	0.67	2.29	0.77 ± 0.06	2.6 ± 0.7
SLD	−177.938	22.790	2.707	−2.479	−180.42	2.704	0.60	2.05	0.65 ± 0.05	2.2 ± 0.6
CCD	−221.315	20.213	2.725	−1.893	−223.21	2.722	0.53	1.69	0.56 ± 0.04	1.9 ± 0.5

a breakdown scale of 3.2 MeV. At this energy there is a level which is outside the ground-state rotational band [124]. The corresponding breakdown spin is $J_b \approx 5$. The EFT results are consistent with the microscopic computations from angular momentum projection. They also agree with data.

The recent computations by Miyagi *et al.* [119] failed to reproduce the collective behavior of ^{34}Mg. Calculated energies of the $J^\pi = 2^+$ states are about a factor 2 too large and $B(E2)$ values are too small. Those calculations were based on a multishell approach including orbitals up to the $1p0f$ shell. Such a model space is probably too small to capture quadrupole collectivity because the mass quadrupole operator couples neutrons in the $1p0f$ shell to the $2p1f0h$ shell.

Our results for the Hartree-Fock basis and a model space with $N_{\max} = 7$ and with the oscillator frequency $\hbar\omega = 20$ MeV are summarized in Table III. Again we see that charge radii only change at the per-mille level under projection.

D. Ground-state properties

Figure 9 shows the energy gain δE from angular-momentum projection within CCD for the nuclei ^{8}Be, ^{20}Ne, and ^{34}Mg. We see that δE is sufficiently converged in the model spaces we employed and only find a small residual dependence on the oscillator spacing. The gain decreases with increasing mass number and is not an extensive quantity.

Figure 10 shows the ground-state energy per nucleon from angular-momentum projected CCD for the nuclei ^{8}Be, ^{20}Ne, and ^{34}Mg. For comparison, projected CCSD for $N_{\max} = 9$ gives a total of ≈100 and ≈400 keV additional binding compared to CCD at the optimal frequency for ^{20}Ne and ^{34}Mg, respectively. Again, the results are sufficiently converged with respect to the employed model spaces. We note that the projection only decreases the ground state energy per particle by about 0.5, 0.17, and 0.08 MeV for ^{8}Be, ^{20}Ne, and ^{34}Mg, respectively.

More accurate ground-state energies require us to include triples cluster excitations. We perform unprojected CCSD and CCSDT-1 computations [126] starting from Hartree-Fock computations in a large single-particle basis with $N_{\max} = 12$. Using the Hartree-Fock basis we then compute natural orbitals from second-order perturbation theory and truncate the basis to a size corresponding to $N_{\max} = 10$ based on the occupation

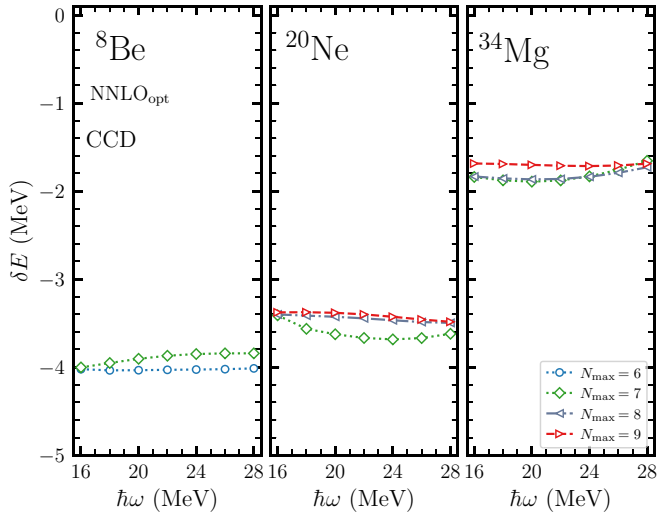

FIG. 9. Gain in ground-state energy from angular-momentum projection for ^{8}Be, ^{20}Ne and ^{34}Mg (from left to right) as a function of the harmonic oscillator spacing for model-space sizes as indicated by $N_{\max}$. Calculations are performed in the CCD approximation.

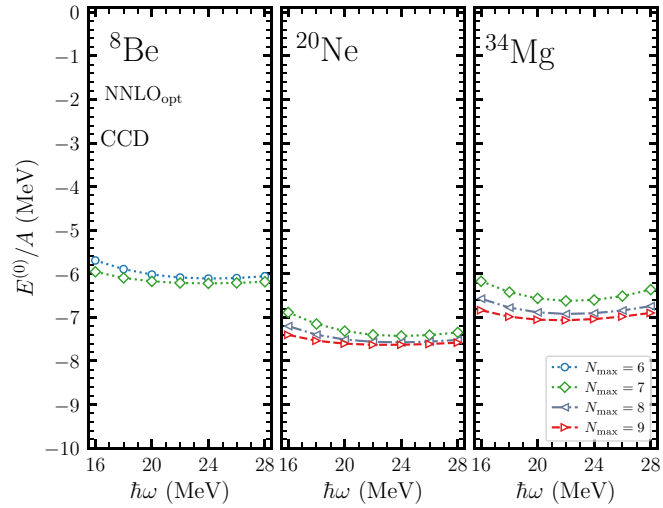

FIG. 10. Projected ground-state energy per nucleon for ^{8}Be, ^{20}Ne and ^{34}Mg (from left to right) as a function of the harmonic oscillator spacing for model-space sizes as indicated by $N_{\max}$. Calculations are performed in the CCD approximation.

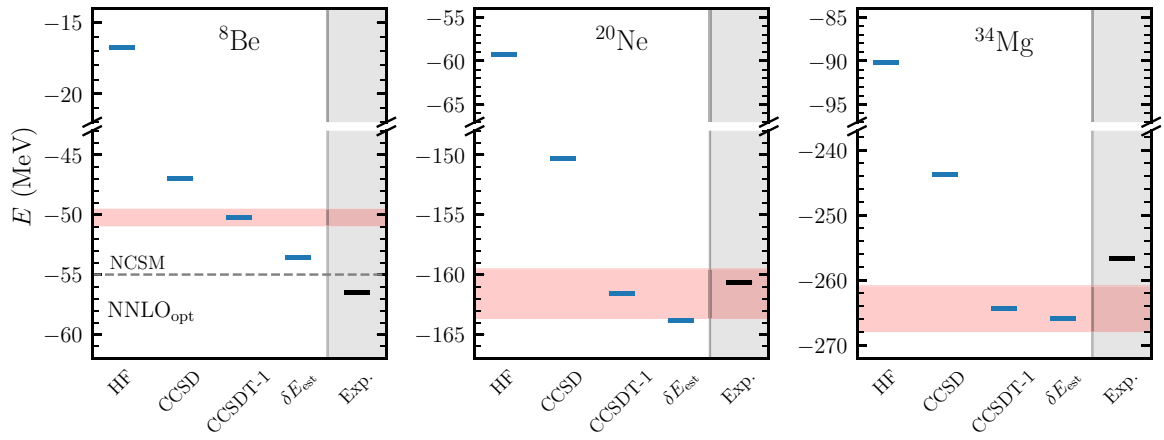

FIG. 11. Ground-state energies of ^{8}Be, ^{20}Ne, and ^{34}Mg shown (from left to right) with unprojected Hartree-Fock, unprojected CCSD, and unprojected CCSDT-1 truncations. The estimated energy gain from angular-momentum projection, $\delta E_{\rm est}$, is based on the leading-order EFT result. The light red band shows the estimated uncertainty at the CCSDT-1 truncation. The NCSM result (dashed line in ^{8}Be) is from an extrapolation to an infinite model space [27]. The right column shows experiment.

numbers with respect to the Fermi surface. For the CCSDT-1 calculations we reduce the number of the 3p-3h amplitudes by an additional cut on occupation numbers; see Refs. [20,85] for details. These calculations yield the correlation energies $\Delta E_{\rm CCSD}$ and $\Delta E_{\rm CCSDT\text{-}1}$ along with the ground-state expectation values $\langle J^2\rangle_{\rm CCSD}$ and $\langle J^2\rangle_{\rm CCSDT\text{-}1}$. Projected ground-state energies can be decomposed as

$$E = E_{\rm ref} + \Delta E_{\rm CCSD} + \Delta E_{\rm CCSDT\text{-}1} + \delta E, \qquad (80)$$

where δE denotes the gain of the ground-state energy from angular-momentum projection. As the projection is presently limited to smaller bases, and we have not performed projection of triples results, we use Eq. (73) to estimate δE based on $\langle J^2\rangle_{\rm CCSDT\text{-}1}$ and the energy spacing $E^{(2)} - E^{(0)}$ based on either SQD or SLD calculations; this estimate is denoted as $\delta E_{\rm est}$ in what follows.

Figure 11 shows how the ground-state energies of ^{8}Be, ^{20}Ne and ^{34}Mg decrease with increasing sophistication of the unprojected many-body computation (from left to right), and with addition of the estimate $\delta E_{\rm est}$ from angular-momentum projection. The light red band shows the estimated uncertainty at the CCSDT-1 truncation (which is about 2% of the total correlation energy). For ^{8}Be, the estimated energy gain from projection is clearly outside the uncertainty estimate from the CCSDT-1 truncation. This is possibly due to the strong α correlations in this unbound nucleus. The ground-state energy of the α particle is -27.76 MeV with the NNLO$_{\rm opt}$ potential [106], and our result (as well as the extrapolated NCSM energy of about -55.0 MeV [27]) is thus above the α-α threshold. We note that the estimated energy gain from projection decreases with increasing mass number. The comparison with experiment (shown as black bars) shows that the NNLO$_{\rm opt}$ interaction overbinds ^{20}Ne and ^{34}Mg.

The computation of $\langle Q_{20}\rangle$ and R^2_{ch} in the unprojected states allows us to compute the nuclear deformation parameter β via Eq. (79). We observe no significant difference between CCSD and CCSDT-1 results. For ^{20}Ne we find $\beta_2 \approx 0.70$, larger than the value $\beta_2 = 0.47$ deduced from experimental data [127]. For ^{34}Mg, we find $\beta_2 \approx 0.57$ and this agrees within experimental uncertainties with the values $\beta_2 = 0.62(6)$ and $\beta_2 = 0.68(16)$ extracted [128] from experimental data in Refs. [124] and [123], respectively. Our results for the ground-state properties of ^{8}Be, ^{20}Ne, and ^{34}Mg are summarized in Table IV.

VII. SHELL-MODEL HAMILTONIANS

We also compared projected coupled-cluster computations with full configuration interaction (FCI) results for the traditional shell-model. We employ the KB3G interaction for pf-shell nuclei [129]. The model space is relatively small and consists of four spherical orbitals above the frozen core of ^{40}Ca. In the nuclear shell model, many-body wave functions typically exhibit strong correlations, and truncated coupled-cluster wave functions do not yield accurate total energies [130], while spectra are more accurate [131].

TABLE IV. Summary of results for ^{8}Be, ^{20}Ne, and ^{34}Mg. Calculations started from a natural orbital basis constructed in a $N_{\rm max} = 12$ model space and truncated to $N^{\rm nat}_{\rm max} = 10$ for the coupled-cluster calculations. We used the oscillator frequencies $\hbar\omega = 24$, 22, and 18 MeV for ^{8}Be, ^{20}Ne, and ^{34}Mg, respectively.

	$E_{\rm ref}$	$\langle J^2\rangle_{\rm ref}$	$\langle Q_2\rangle_{\rm ref}$	$\Delta E_{\rm SD}$	$\langle J^2\rangle_{\rm SD}$	$\langle Q_2\rangle_{\rm SD}$	$\Delta E_{\rm SDT-1}$	$\langle J^2\rangle_{\rm SDT-1}$	$\langle Q_2\rangle_{\rm SDT-1}$	$\delta E_{\rm est}$	E	$E_{\rm Expt.}$
^{8}Be	−16.74	11.17	19.46	−30.26	6.69	19.64	−3.24	5.82	18.86	−3.33	−53.58	−56.50
^{20}Ne	−59.62	21.26	35.84	−91.06	14.71	36.34	−11.27	12.09	35.71	−2.26	−164.21	−160.64
^{34}Mg	−90.21	22.62	38.56	−153.57	18.40	38.38	−20.56	15.03	36.97	−1.50	−265.84	−256.71

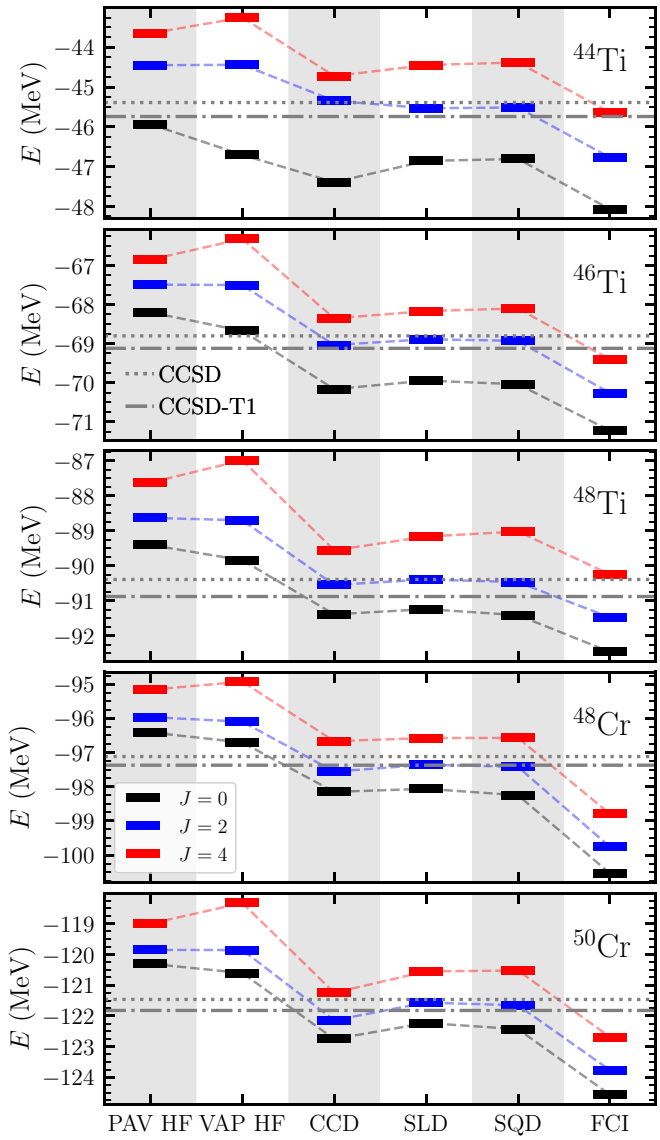

FIG. 12. Low-lying states with spin J of selected pf-shell nuclei computed with projection-after-variation Hartree-Fock (PAV HF), variation-after-projection Hartree-Fock (VAP HF), and projected CCD, SLD, and SQD methods, and compared to FCI results. Horizontal lines shown are the ground-state energies from unprojected coupled-cluster computations.

Figure 12 compares various projection techniques with exact FCI results for the nuclei ^{44}Ti, ^{46}Ti, ^{48}Ti, ^{48}Cr, and ^{50}Cr. The Hartree-Fock energies lack several MeV of binding, and the VAP results for the spectrum are not more accurate than those from PAV. Including correlations beyond Hartree-Fock significantly lowers the ground-state energies, as shown by the CCD, SLD, and SQD results, and the spectra also improve. The spacings of the SQD spectra are close to the FCI results. The dotted and dashed-dotted horizontal lines show the results from single-reference CCSD and CCSDT-1, respectively. We see that projected SLD and SQD results improve on these ground-state energies, and CCD results gain the most energy. We attribute the difference between the projected coupled-cluster and FCI results to lacking many-particle–many-hole excitations.

VIII. SUMMARY

We performed angular-momentum projection after variation within coupled-cluster theory using two different approaches. The first is based on the non-Hermitian energy functional of coupled-cluster theory and projects within the disentangled formalism via ordinary differential equations. This approach scales favorably and yields somewhat too compressed spectra when compared with benchmarks. We expect that more accurate projections could be achieved within a bi-variational energy functional, i.e., using a more sophisticated parametrization of the bra state. Furthermore, we also expect improvements from inclusion of W_3 in the differential equations. The second approach employs truncated coupled-cluster wave functions within a Hermitian energy functional. We studied a linear and a quadratic truncation of the doubles cluster operator. The latter is numerically very expensive. Spectra are more accurate than in the non-Hermitian approach. Benchmark calculations for ^{8}Be and ^{20}Ne based on a chiral nucleon-nucleon potential show that the angular momentum projections are fairly accurate. Comparing with traditional shell-model calculation of pf-shell nuclei revealed the more accurate reproduction of spectra within the Hermitian approach and the larger ground-state energy gain within the non-Hermitian approach. The computed ground-state rotational band of the exotic nucleus ^{34}Mg agrees with experimental data. This opens the avenue to perform *ab initio* predictions of rotational properties in medium-mass exotic nuclei.

We used our microscopic results to compute the low-energy constants of the rigid-rotor model (which is the leading order Hamiltonian within an effective theory of nuclear rotation) and estimated uncertainties from omitted higher-order corrections. The effective theory accurately reproduces rotational bands.

The ground-state energy gained from angular-momentum projection decreases with increasing mass number, and this is understood within the effective theory. Thus, such corrections can be computed using methods that are not size extensive. Computations of charge radii revealed that projections have only little impact on this observable.

The Department of Energy will provide public access to these results of federally sponsored research in accordance with the DOE Public Access Plan [132].

ACKNOWLEDGMENTS

We thank T. M. Henderson for many useful discussions and for sharing his numerical programs with us. We also thank T. D. Morris for many useful discussions, and M. Caprio and K. Launey for sharing their results with us. This work was supported by the U.S. Department of Energy, Office of Science, Office of Nuclear Physics, under Awards No. DE-FG02-96ER40963 and No. DE-SC0018223. A.T. was supported in part by the Deutsche Forschungsgemeinschaft

(DFG, German Research Foundation), Project-ID 279384907, SFB 1245 and by the European Research Council (ERC) under the European Union's Horizon 2020 Research and Innovation Programme (Grant Agreement No. 101020842). Computer time was provided by the Innovative and Novel Computational Impact on Theory and Experiment (INCITE) programme. This research used resources of the Oak Ridge Leadership Computing Facility located at Oak Ridge National Laboratory, which is supported by the Office of Science of the Department of Energy and is managed by UT-Battelle, LLC, under contract No. DE-AC05-00OR22725. The U.S. Government retains and the publisher, by accepting the article for publication, acknowledges that the U.S. Government retains a non-exclusive, paid-up, irrevocable, worldwide license to publish or reproduce the published form of this manuscript, or allow others to do so, for U.S. Government purposes.

APPENDIX A: TRANSFORMED OPERATORS

1. Computation of $\breve{O}$

Considering an arbitrary operator O, we are interested in computing its similarity-transformed partner

$$\breve{O} \equiv e^{-Z} O e^{Z}, \tag{A1}$$

where Z is a one-body operator $Z \equiv \sum_{pq} z_{pq} c_p^\dagger c_q$. Because of the one-body nature of Z, the Baker-Campbell-Hausdorff expansion is simple and one finds

$$e^{-Z} c_p e^{Z} = \sum_q [e^Z]_{pq} c_q, \tag{A2a}$$

$$e^{-Z} c_p^\dagger e^{Z} = \sum_q c_q^\dagger [e^{-Z}]_{qp}. \tag{A2b}$$

Here and in what follows, the matrix of a single-particle operator is denoted using brackets.

The transformation is thus represented by a matrix exponential that takes a particularly simple form for $Z \equiv T_1$. Let us first provide the matrix representation of T_1

$$[T_1] = \begin{pmatrix} t_{hh} & t_{hp} \\ t_{ph} & t_{pp} \end{pmatrix} \equiv \begin{pmatrix} 0 & 0 \\ t & 0 \end{pmatrix}, \tag{A3}$$

where the one-body basis has been separated into occupied (hole) and unoccupied (particle) states in $|\Phi\rangle$. Because T_1 [Eq. (10)] is a pure excitation operator, only the particle-hole block t differs from zero.

Given Eq. (A3), the matrix exponential that transforms one-body annihilation operators reads as

$$[e^{T_1}] = [1 + T_1] = \begin{pmatrix} 1 & 0 \\ t & 1 \end{pmatrix}, \tag{A4}$$

whereas the one transforming one-body creation operators is

$$[e^{-T_1}] = [1 - T_1] = \begin{pmatrix} 1 & 0 \\ -t & 1 \end{pmatrix}. \tag{A5}$$

In order to illustrate how Eq. (A1) eventually operates, let us consider a one-body operator

$$O \equiv \sum_{pq} o_{pq} c_p^\dagger c_q, \tag{A6}$$

as an example. Given Eq. (A2), the similarity-transformed operator is itself a one-body operator

$$\breve{O} \equiv \sum_{pq} \breve{o}_{pq} c_p^\dagger c_q, \tag{A7}$$

whose matrix elements are

$$\begin{aligned} \breve{o}_{pq} &\equiv [\breve{O}]_{pq} \\ &= \sum_{rs} [e^{-T_1}]_{pr} [O]_{rs} [e^{T_1}]_{sq}, \end{aligned} \tag{A8}$$

i.e., to each ket and bra index of the initial operator's matrix elements we associate a right and left multiplication with matrix (A4) and (A5), respectively.

2. Computation of $\tilde{O}$

We consider an arbitrary operator O and want to compute

$$\tilde{O} \equiv e^{V} \mathcal{R}^{-1}(\beta) O \mathcal{R}(\beta) e^{-V}, \tag{A9}$$

where the modified rotation operator is given by

$$\mathcal{R}(\beta) \equiv e^{T_1^\dagger} R(\beta) e^{T_1}. \tag{A10}$$

This similarity transformation was used in Eq. (51). The operator $\tilde{O}$ thus results from four successive elementary transformations as described in Appendix A 1, taking successively $Z \equiv T_1^\dagger$, $Z \equiv -i\beta J_y$, $Z \equiv T_1$, and $Z \equiv -V$. Each of these transformations corresponds to a change of the single-particle basis. The third transformation corresponds to the case worked out in Appendix A 1. The first one is deduced from it by taking the Hermitian conjugate of matrices (A4) and (A5). The second transformation has the matrix elements $[R(\beta)]_{pr}$ of $R(\beta)$ in the Hartree-Fock basis. These matrix elements can be obtained from the initial matrix elements of $R(\beta)$ in the spherical single-particle basis [Eq. (18)] via the Hartree-Fock transformation. Thus, the first three transformations multiply each ket index of the original matrix elements from the right by the matrix

$$[\mathcal{R}(\beta)] = \begin{pmatrix} 1 & t^\dagger \\ 0 & 1 \end{pmatrix} [R(\beta)] \begin{pmatrix} 1 & 0 \\ t & 1 \end{pmatrix}, \tag{A11}$$

and each bra index from the left by the matrix

$$\left[\mathcal{R}^{-1}(\beta)\right] = \begin{pmatrix} 1 & 0 \\ -t & 1 \end{pmatrix} [R(-\beta)] \begin{pmatrix} 1 & -t^\dagger \\ 0 & 1 \end{pmatrix}. \tag{A12}$$

Finally, we need to work out the fourth transformation associated with $Z \equiv -V$. Decomposing Eq. (A11) according to

$$[\mathcal{R}(\beta)] = \begin{pmatrix} \mathcal{R}_{hh} & \mathcal{R}_{hp} \\ \mathcal{R}_{ph} & \mathcal{R}_{pp} \end{pmatrix}, \tag{A13}$$

the matrix associated with the operator V reads [55]

$$[V] \equiv \begin{pmatrix} 0 & v_{hp} \\ 0 & 0 \end{pmatrix} \tag{A14}$$

with

$$v_{hp} = (\mathcal{R}_{hh})^{-1} \mathcal{R}_{hp} \equiv v. \tag{A15}$$

Thus, the similarity transformation is worked out such that to each ket index of the initial matrix elements is associated a right multiplication with the matrix

$$\begin{pmatrix} 1 & -v \\ 0 & 1 \end{pmatrix}, \tag{A16}$$

and to each bra index is associated a left multiplication with the matrix

$$\begin{pmatrix} 1 & v \\ 0 & 1 \end{pmatrix}. \tag{A17}$$

APPENDIX B: MANY-BODY MATRIX ELEMENTS

1. Operator $\overline{U}$

In Sec. IV C 5, the Hamiltonian and norm kernels where expressed in terms of the matrix elements of the excitation part of the similarity-transformed disconnected excitation operator $\overline{U}$:

$$u^{a_1 a_2 \cdots}_{i_1 i_2 \cdots} = \left\langle \Phi^{a_1 a_2 \cdots}_{i_1 i_2 \cdots} \middle| \overline{U} | \Phi \right\rangle. \tag{B1}$$

The expressions of these matrix elements up to 4p-4h are

$$\overline{U}^{(0)} = 1 + \overline{T}_2^{(0)} + \frac{1}{2}\left(\sum_{ia} \tau_a^i \tau_i^a + \frac{1}{4} \sum_{ijab} \bar{t}_{ab}^{ij} \bar{t}_{ij}^{ab} \right), \tag{B2a}$$

$$\overline{u}_i^a = \left(1 + \frac{1}{2}\overline{T}_2^{(0)}\right)\tau_i^a + \frac{1}{2}\left(\sum_c \tau_c^a \tau_i^c - \sum_k \tau_k^a \tau_i^k + \sum_{kc} \bar{t}_{ik}^{ac} \tau_c^k + \sum_{kc} \bar{t}_{ic}^{ak} \tau_k^c + \frac{1}{2} \sum_{cdk} \bar{t}_{cd}^{ak} \bar{t}_{ik}^{cd} - \frac{1}{2} \sum_{ckl} \bar{t}_{kl}^{ac} \bar{t}_{ic}^{kl} \right), \tag{B2b}$$

$$\begin{aligned} \overline{u}_{ij}^{ab} = {} & \left(1 + \frac{1}{2}\overline{T}_2^{(0)}\right)\bar{t}_{ij}^{ab} + P(ab)\tau_i^a \tau_j^b + \frac{1}{2}\Bigg(P(ab) \sum_c \bar{t}_{ij}^{ac} \tau_c^b - P(ij) \sum_k \bar{t}_{ik}^{ab} \tau_j^k + P(ij) \sum_c \bar{t}_{ic}^{ab} \tau_j^c - P(ab) \sum_k \bar{t}_{ij}^{ak} \tau_k^b \\ & + P(ab)P(ij) \sum_{kc} \bar{t}_{ik}^{ac} \bar{t}_{cj}^{kb} + \frac{1}{2} \sum_{kl} \bar{t}_{kl}^{ab} \bar{t}_{ij}^{kl} + \frac{1}{2} \sum_{cd} \bar{t}_{cd}^{ab} \bar{t}_{ij}^{cd} \Bigg), \end{aligned} \tag{B2c}$$

$$\begin{aligned} \overline{u}_{ijk}^{abc} &= P(ab/c)P(ij/k)\bar{t}_{ij}^{ab} \tau_k^c + \frac{1}{2} P(ab/c)P(ij/k) \left(\sum_d \bar{t}_{ij}^{cd} \bar{t}_{dk}^{ab} - \sum_l \bar{t}_{kl}^{ab} \bar{t}_{ij}^{lc} \right) \\ &= P(ab/c)P(ij/k) \left(\bar{t}_{ij}^{ab} \tau_k^c - \sum_l \bar{t}_{kl}^{ab} \bar{t}_{ij}^{lc} \right), \end{aligned} \tag{B2d}$$

$$\overline{u}_{ijkl}^{abcd} = \frac{1}{2} P(ab/cd)P(ij/kl) \bar{t}_{ij}^{ab} \bar{t}_{kl}^{cd}. \tag{B2e}$$

Here P denotes the permutation operator [84]. In Eq. (B2d) the sum over d is the negative of the sum over l after antisymmetrization, as can be shown by writing out the explicit similarity transformations of T_2.

Employing the SLD approximation leads to $U = (1 + T_2)$ such that the matrix elements beyond rank two vanish. In this case, the above expressions reduce to $\overline{U}^{(0)} = 1 + \overline{T}_2^{(0)}$, $\overline{u}_i^a = \tau_i^a$, and $\overline{u}_{ij}^{ab} = \bar{t}_{ij}^{ab}$.

2. Operator $\overline{HU}$

Similarly, the matrix elements

$$\overline{x}^{a_1 a_2 \cdots}_{i_1 i_2 \cdots} = \left\langle \Phi^{a_1 a_2 \cdots}_{i_1 i_2 \cdots} \middle| \overline{HU} | \Phi \right\rangle \tag{B3}$$

are needed up to 4p-4h excitation level. These are

$$\overline{X}^{(0)} = \overline{H}^{(0)}\overline{U}^{(0)} + \sum_{ia} \overline{h}_a^i \overline{u}_i^a + \frac{1}{4} \sum_{ijab} \overline{h}_{ab}^{ij} \overline{u}_{ij}^{ab}, \tag{B4a}$$

$$\overline{x}_i^a = \overline{H}^{(0)}\overline{u}_i^a + \overline{h}_i^a \overline{U}^{(0)} + \sum_{bj} \overline{h}_{ib}^{aj} \overline{u}_j^b + \sum_b \overline{h}_b^a \overline{u}_i^b + \sum_{bj} \overline{h}_{ib}^{aj} \overline{u}_j^b + \frac{1}{2} \sum_{bcj} \overline{h}_{bc}^{aj} \overline{u}_{ij}^{bc} - \frac{1}{2} \sum_{bjk} \overline{h}_{ib}^{jk} \overline{u}_{jk}^{ab} + \sum_{bj} \overline{h}_b^j \overline{u}_{ij}^{ab} + \frac{1}{4} \sum_{bcjk} \overline{h}_{jk}^{bc} \overline{u}_{ijk}^{abc}, \tag{B4b}$$

$$\overline{x}_{ij}^{ab} = \overline{H}^{(0)}\overline{u}_{ij}^{ab} + \overline{h}_{ij}^{ab}\overline{U}^{(0)} + P(ab)P(ij)\overline{h}_i^a \overline{u}_j^b + P(ab) \sum_c \overline{h}_c^b \overline{u}_{ij}^{ac} - P(ij) \sum_k \overline{h}_j^k \overline{u}_{ik}^{ab} + \frac{1}{2} \sum_{cd} \overline{h}_{cd}^{ab} \overline{u}_{ij}^{cd}$$

$$\frac{1}{2}\sum_{kl}\overline{h}_{ij}^{kl}\overline{u}_{kl}^{ab}+P(ab)P(ij)\sum_{ck}\overline{h}_{cj}^{kb}\overline{u}_{ik}^{ac}+P(ij)\sum_{c}\overline{h}_{cj}^{ab}\overline{u}_{i}^{c}-P(ab)\sum_{k}\overline{h}_{ij}^{kb}\overline{u}_{k}^{a}+\sum_{ck}\overline{h}_{c}^{k}\overline{u}_{ijk}^{abc}+P(ab)\frac{1}{2}\sum_{cdk}\overline{h}_{cd}^{bk}\overline{u}_{ijk}^{acd}$$
$$-P(ij)\frac{1}{2}\sum_{ckl}\overline{h}_{jc}^{kl}\overline{u}_{ikl}^{abc}+\frac{1}{4}\sum_{cdkl}\overline{h}_{cd}^{kl}\overline{u}_{ijkl}^{abcd}, \tag{B4c}$$

$$\overline{x}_{ijk}^{abc}=\overline{H}^{(0)}\overline{u}_{ijk}^{abc}+P(ab/c)P(ij/k)\left(\overline{h}_{ij}^{ab}\overline{u}_{k}^{c}+\overline{u}_{ij}^{ab}\overline{h}_{k}^{c}\right)+P(ab/c)\sum_{d}\overline{u}_{ijk}^{abd}\overline{h}_{d}^{c}-P(ij/k)\sum_{l}\overline{u}_{ijl}^{abc}\overline{h}_{k}^{l}$$
$$+\frac{1}{2}P(ab/c)\sum_{de}\overline{u}_{ijk}^{dec}\overline{h}_{de}^{ab}+\frac{1}{2}P(ij/k)\sum_{lm}\overline{u}_{lmk}^{abc}\overline{h}_{ij}^{lm}+P(ij/k)P(ab/c)\left(\sum_{dl}\overline{u}_{ijl}^{abd}\overline{h}_{dk}^{lc}+\sum_{d}\overline{u}_{ij}^{cd}\overline{h}_{dk}^{ab}-\sum_{l}\overline{u}_{kl}^{ab}\overline{h}_{ij}^{lc}\right)$$
$$+\sum_{dl}\overline{u}_{ijkl}^{abcd}\overline{h}_{d}^{k}+\frac{1}{2}P(ab/c)\sum_{del}\overline{u}_{ijkl}^{abde}\overline{h}_{de}^{cl}-\frac{1}{2}P(ij/k)\sum_{dlm}\overline{u}_{ijlm}^{abcd}\overline{h}_{kd}^{lm}, \tag{B4d}$$

$$\overline{x}_{ijkl}^{abcd}=\overline{H}^{(0)}\overline{u}_{ijkl}^{abcd}+P(ab/cd)P(ij/kl)\overline{h}_{ij}^{ab}\overline{u}_{kl}^{cd}+P(abc/d)P(ijk/l)\left(\overline{h}_{l}^{d}\overline{u}_{ijk}^{abc}+\sum_{em}\overline{u}_{ijkm}^{abce}\overline{h}_{el}^{md}\right)$$
$$+P(abc/d)\sum_{e}\overline{h}_{e}^{d}\overline{u}_{ijkl}^{abce}-P(ijk/l)\sum_{m}\overline{h}_{l}^{m}\overline{u}_{ijkm}^{abcd}+\frac{1}{2}P(ab/cd)\sum_{ef}\overline{u}_{ijkl}^{abef}\overline{h}_{ef}^{cd}+\frac{1}{2}P(ij/kl)\sum_{mn}\overline{u}_{ijmn}^{abcd}\overline{h}_{kl}^{mn}$$
$$+P(ab/cd)P(ijk/l)\sum_{e}\overline{u}_{ijk}^{abe}\overline{h}_{el}^{cd}-P(abc/d)P(ij/kl)\sum_{m}\overline{u}_{ijm}^{abc}\overline{h}_{kl}^{md}. \tag{B4e}$$

Here $\overline{H}^{(0)}$, $\overline{h}_{q}^{p}$, and $\overline{h}_{rs}^{pq}$ denote the matrix elements of the normal-ordered zero-, one-, and two-body parts of $\overline{H}$, respectively.

[1] K. W. Schmid, Z. Ren-Rong, F. Grümmer, and A. Faessler, Beyond symmetry-projected quasi-particle mean fields: A new variational procedure for nuclear structure calculations, Nucl. Phys. A **499**, 63 (1989).

[2] M. Bender, P.-H. Heenen, and P.-G. Reinhard, Self-consistent mean-field models for nuclear structure, Rev. Mod. Phys. **75**, 121 (2003).

[3] J. A. Sheikh, J. J. Dobaczewski, P. Ring, L. M. Robledo, and C. Yannouleas, Symmetry restoration in mean-field approaches, J. Phys. G: Nucl. Part. Phys. **48**, 123001 (2021).

[4] H. Kümmel, K. H. Lührmann, and J. G. Zabolitzky, Many-fermion theory in expS- (or coupled cluster) form, Phys. Rep. **36**, 1 (1978).

[5] G. Hagen, T. Papenbrock, M. Hjorth-Jensen, and D. J. Dean, Coupled-cluster computations of atomic nuclei, Rep. Prog. Phys. **77**, 096302 (2014).

[6] K. Tsukiyama, S. K. Bogner, and A. Schwenk, In-Medium Similarity Renormalization Group For Nuclei, Phys. Rev. Lett. **106**, 222502 (2011).

[7] H. Hergert, S. K. Bogner, T. D. Morris, A. Schwenk, and K. Tsukiyama, The in-medium similarity renormalization group: A novel *ab initio* method for nuclei, Phys. Rep. **621**, 165 (2016).

[8] S. R. Stroberg, A. Calci, H. Hergert, J. D. Holt, S. K. Bogner, R. Roth, and A. Schwenk, Nucleus-Dependent Valence-Space Approach to Nuclear Structure, Phys. Rev. Lett. **118**, 032502 (2017).

[9] S. R. Stroberg, H. Hergert, S. K. Bogner, and J. D. Holt, Nonempirical interactions for the nuclear shell model: An update, Annu. Rev. Nucl. Part. Sci. **69**, 307 (2019).

[10] S. R. Stroberg, J. D. Holt, A. Schwenk, and J. Simonis, *Ab Initio* Limits of Atomic Nuclei, Phys. Rev. Lett. **126**, 022501 (2021).

[11] M. Heinz, A. Tichai, J. Hoppe, K. Hebeler, and A. Schwenk, In-medium similarity renormalization group with three-body operators, Phys. Rev. C **103**, 044318 (2021).

[12] W.H. Dickhoff and C. Barbieri, Self-consistent Green's function method for nuclei and nuclear matter, Prog. Part. Nucl. Phys. **52**, 377 (2004).

[13] V. Somà, C. Barbieri, and T. Duguet, *Ab initio* Gorkov-Green's function calculations of open-shell nuclei, Phys. Rev. C **87**, 011303(R) (2013).

[14] J. D. Holt, J. Menéndez, J. Simonis, and A. Schwenk, Three-nucleon forces and spectroscopy of neutron-rich calcium isotopes, Phys. Rev. C **90**, 024312 (2014).

[15] A. Tichai, J. Langhammer, S. Binder, and R. Roth, Hartree-Fock many-body perturbation theory for nuclear ground-states, Phys. Lett. B **756**, 283 (2016).

[16] B. S. Hu, F. R. Xu, Z. H. Sun, J. P. Vary, and T. Li, *Ab initio* nuclear many-body perturbation calculations in the Hartree-Fock basis, Phys. Rev. C **94**, 014303 (2016).

[17] A. Tichai, P. Arthuis, T. Duguet, H. Hergert, V. Somà, and R. Roth, Bogoliubov many-body perturbation theory for open-shell nuclei, Phys. Lett. B **786**, 195 (2018).

[18] A. Tichai, E. Gebrerufael, K. Vobig, and R. Roth, Open-shell nuclei from no-core shell model with perturbative improvement, Phys. Lett. B **786**, 448 (2018).

[19] A. Tichai, R. Roth, and T. Duguet, Many-body perturbation theories for finite nuclei, Front. Phys. **8**, 164 (2020).

[20] S. J. Novario, G. Hagen, G. R. Jansen, and T. Papenbrock, Charge radii of exotic neon and magnesium isotopes, Phys. Rev. C **102**, 051303(R) (2020).

[21] V. Somà, C. Barbieri, T. Duguet, and P. Navrátil, Moving away from singly-magic nuclei with Gorkov Green's function theory, Eur. Phys. J. A **57**, 135 (2021).

[22] E. Caurier, G. Martínez-Pinedo, F. Nowack, A. Poves, and A. P. Zuker, The shell model as a unified view of nuclear structure, Rev. Mod. Phys. **77**, 427 (2005).

[23] E. Caurier, J. Menéndez, F. Nowacki, and A. Poves, Coexistence of spherical states with deformed and superdeformed bands in doubly magic ^{40}Ca: A shell-model challenge, Phys. Rev. C **75**, 054317 (2007).

[24] M. A. Caprio, P. Maris, and J. P. Vary, Emergence of rotational bands in ab initio no-core configuration interaction calculations of light nuclei, Phys. Lett. B **719**, 179 (2013).

[25] G. R. Jansen, J. Engel, G. Hagen, P. Navratil, and A. Signoracci, *Ab Initio* Coupled-Cluster Effective Interactions for the Shell Model: Application to Neutron-Rich Oxygen and Carbon Isotopes, Phys. Rev. Lett. **113**, 142502 (2014).

[26] S. K. Bogner, H. Hergert, J. D. Holt, A. Schwenk, S. Binder, A. Calci, J. Langhammer, and R. Roth, Nonperturbative Shell-Model Interactions from the In-Medium Similarity Renormalization Group, Phys. Rev. Lett. **113**, 142501 (2014).

[27] M. A. Caprio, P. Maris, J. P. Vary, and R. Smith, Collective rotation from ab initio theory, Int. J. Mod. Phys. E **24**, 1541002 (2015).

[28] P. Maris, M. A. Caprio, and J. P. Vary, Emergence of rotational bands in *ab initio* no-core configuration interaction calculations of the Be isotopes, Phys. Rev. C **91**, 014310 (2015).

[29] N. Shimizu, T. Abe, Y. Tsunoda, Y. Utsuno, T. Yoshida, T. Mizusaki, M. Honma, and T. Otsuka, New-generation Monte Carlo shell model for the K computer era, Prog. Theor. Exp. Phys. **2012**, 01A205 (2012).

[30] T. Dytrych, K. D. Launey, J. P. Draayer, P. Maris, J. P. Vary, E. Saule, U. Catalyurek, M. Sosonkina, D. Langr, and M. A. Caprio, Collective Modes in Light Nuclei from First Principles, Phys. Rev. Lett. **111**, 252501 (2013).

[31] T. Dytrych, K. D. Launey, J. P. Draayer, D. J. Rowe, J. L. Wood, G. Rosensteel, C. Bahri, D. Langr, and R. B. Baker, Physics of Nuclei: Key Role of an Emergent Symmetry, Phys. Rev. Lett. **124**, 042501 (2020).

[32] T. Papenbrock, Effective theory for deformed nuclei, Nucl. Phys. A **852**, 36 (2011).

[33] E. A. Coello Pérez and T. Papenbrock, Effective theory for the nonrigid rotor in an electromagnetic field: Toward accurate and precise calculations of $e2$ transitions in deformed nuclei, Phys. Rev. C **92**, 014323 (2015).

[34] Q. B. Chen, N. Kaiser, Ulf-G. Meißner, and J. Meng, Effective field theory for triaxially deformed nuclei, Eur. Phys. J. A **53**, 204 (2017).

[35] T. Papenbrock and H. A. Weidenmüller, Effective field theory for deformed odd-mass nuclei, Phys. Rev. C **102**, 044324 (2020).

[36] I. K. Alnamlah, E. A. Coello Pérez, and D. R. Phillips, Effective field theory approach to rotational bands in odd-mass nuclei, Phys. Rev. C **104**, 064311 (2021).

[37] N. Paar, D. Vretenar, E. Khan, and G. Colò, Exotic modes of excitation in atomic nuclei far from stability, Rep. Prog. Phys. **70**, R02 (2007).

[38] J. Erler, N. Birge, M. Kortelainen, W. Nazarewicz, E. Olsen, A. M. Perhac, and M. Stoitsov, The limits of the nuclear landscape, Nature (London) **486**, 509 (2012).

[39] S. Goriely, N. Chamel, and J. M. Pearson, Skyrme-Hartree-Fock-Bogoliubov Nuclear Mass Formulas: Crossing the 0.6 MeV Accuracy Threshold with Microscopically Deduced Pairing, Phys. Rev. Lett. **102**, 152503 (2009).

[40] T. Nikšić, D. Vretenar, and P. Ring, Relativistic nuclear energy density functionals: Mean-field and beyond, Prog. Part. Nucl. Phys. **66**, 519 (2011).

[41] S. Shen, H. Liang, W. H. Long, J. Meng, and P. Ring, Towards an *ab initio* covariant density functional theory for nuclear structure, Prog. Part. Nucl. Phys. **109**, 103713 (2019).

[42] U. Van Kolck, Effective field theory of nuclear forces, Prog. Part. Nucl. Phys. **43**, 337 (1999).

[43] E. Epelbaum, H. Krebs, and U.-G. Meißner, Δ-excitations and the three-nucleon force, Nucl. Phys. A **806**, 65 (2008).

[44] R. Machleidt and D.R. Entem, Chiral effective field theory and nuclear forces, Phys. Rep. **503**, 1 (2011).

[45] S. Binder, J. Langhammer, A. Calci, and R. Roth, *Ab initio* path to heavy nuclei, Phys. Lett. B **736**, 119 (2014).

[46] G. Hagen, G. R. Jansen, and T. Papenbrock, Structure of ^{78}Ni from First-Principles Computations, Phys. Rev. Lett. **117**, 172501 (2016).

[47] T. D. Morris, J. Simonis, S. R. Stroberg, C. Stumpf, G. Hagen, J. D. Holt, G. R. Jansen, T. Papenbrock, R. Roth, and A. Schwenk, Structure of the Lightest Tin Isotopes, Phys. Rev. Lett. **120**, 152503 (2018).

[48] B. Hu, W. Jiang, T. Miyagi, Z. Sun, A. Ekström, C. Forssén, G. Hagen, J. D. Holt, T. Papenbrock, S. Ragnar Stroberg, and I. Vernon, *Ab initio* predictions link the neutron skin of ^{208}Pb to nuclear forces, arXiv:2112.01125

[49] R. J. Bartlett and M. Musiał, Coupled-cluster theory in quantum chemistry, Rev. Mod. Phys. **79**, 291 (2007).

[50] H. Hergert, S. K. Bogner, T. D. Morris, S. Binder, A. Calci, J. Langhammer, and R. Roth, *Ab initio* multireference in-medium similarity renormalization group calculations of even calcium and nickel isotopes, Phys. Rev. C **90**, 041302(R) (2014).

[51] M. Frosini, T. Duguet, J.-P. Ebran, and V. Somà, Multi-reference many-body perturbation theory for nuclei, Eur. Phys. J. A **58**, 62 (2022).

[52] M. Frosini, T. Duguet, J.-P. Ebran, B. Bally, T. Mongelli, T. R. Rodríguez, R. Roth, and V. Somà, Multi-reference many-body perturbation theory for nuclei. II. *Ab initio* study of neon isotopes via PGCM and IM-NCSM calculations, Eur. Phys. J. A **58**, 63 (2022).

[53] M. Frosini, T. Duguet, J.-P. Ebran, B. Bally, H. Hergert, T. R. Rodríguez, R. Roth, J. Yao, and V. Somà, Multi-reference many-body perturbation theory for nuclei. III. *Ab initio* calculations at second order in PGCM-PT, Eur. Phys. J. A **58**, 64 (2022).

[54] T. Duguet, Symmetry broken and restored coupled-cluster theory: I. Rotational symmetry and angular momentum, J. Phys. G: Nucl. Part. Phys. **42**, 025107 (2015).

[55] Y. Qiu, T. M. Henderson, J. Zhao, and G. E. Scuseria, Projected coupled cluster theory, J. Chem. Phys. **147**, 064111 (2017).

[56] T. Duguet and A. Signoracci, Symmetry broken and restored coupled-cluster theory. II. Global gauge symmetry and particle

number, J. Phys. G: Nucl. Part. Phys. **44**, 015103 (2017); Erratum: Symmetry broken and restored coupled-cluster theory: II. Global gauge symmetry and particle number (J. Phys. G: Nucl. Part. Phys. 44, 015103 2017) **44**, 049601 (2017).

[57] Y. Qiu, T. M. Henderson, J. Zhao, and G. E. Scuseria, Projected coupled cluster theory: Optimization of cluster amplitudes in the presence of symmetry projection, J. Chem. Phys. **149**, 164108 (2018).

[58] Y. Qiu, T. M. Henderson, T. Duguet, and G. E. Scuseria, Particle-number projected Bogoliubov-coupled-cluster theory: Application to the pairing Hamiltonian, Phys. Rev. C **99**, 044301 (2019).

[59] T. Tsuchimochi and S. L. Ten-no, Orbital-invariant spin-extended approximate coupled-cluster for multi-reference systems, J. Chem. Phys. **149**, 044109 (2018).

[60] T. Mizusaki and P. Schuck, Symmetry projection to coupled-cluster singles plus doubles wave function through the Monte Carlo method, Phys. Rev. C **104**, L031305 (2021).

[61] J. Arponen, Variational principles and linked-cluster exp S expansions for static and dynamic many-body problems, Ann. Phys. (NY) **151**, 311 (1983).

[62] J. S. Arponen, R. F. Bishop, and E. Pajanne, Extended coupled-cluster method. I. Generalized coherent bosonization as a mapping of quantum theory into classical Hamiltonian mechanics, Phys. Rev. A **36**, 2519 (1987).

[63] T. Van Voorhis and M. Head-Gordon, The quadratic coupled cluster doubles model, Chem. Phys. Lett. **330**, 585 (2000).

[64] Edward F. C. Byrd, T. Van Voorhis, and M. Head-Gordon, Quadratic coupled-cluster doubles: Implementation and assessment of perfect pairing optimized geometries, J. Phys. Chem. B **106**, 8070 (2002).

[65] R. J. Bartlett and J. Noga, The expectation value coupled-cluster method and analytical energy derivatives, Chem. Phys. Lett. **150**, 29 (1988).

[66] Péter G. Szalay, M. Nooijen, and R. J. Bartlett, Alternative ansätze in single reference coupled-cluster theory. III. A critical analysis of different methods, J. Chem. Phys. **103**, 281 (1995).

[67] W. Duch and G. H. F. Diercksen, Size-extensivity corrections in configuration interaction methods, J. Chem. Phys. **101**, 3018 (1994).

[68] E. Ramos-Cordoba, P. Salvador, and E. Matito, Separation of dynamic and nondynamic correlation, Phys. Chem. Chem. Phys. **18**, 24015 (2016).

[69] G. F. Bertsch, T. Kawano, and L. M. Robledo, Angular momentum of fission fragments, Phys. Rev. C **99**, 034603 (2019).

[70] J. Fujita and H. Miyazawa, Pion theory of three-body forces, Prog. Theor. Phys. **17**, 360 (1957).

[71] P. F. Bedaque, H.-W. Hammer, and U. van Kolck, Renormalization of the Three-Body System with Short-Range Interactions, Phys. Rev. Lett. **82**, 463 (1999).

[72] E. Epelbaum, H.-W. Hammer, and Ulf-G. Meißner, Modern theory of nuclear forces, Rev. Mod. Phys. **81**, 1773 (2009).

[73] H.-W. Hammer, A. Nogga, and A. Schwenk, *Colloquium*: Three-body forces: From cold atoms to nuclei, Rev. Mod. Phys. **85**, 197 (2013).

[74] A. Bohr and B. R. Mottelson, *Nuclear Structure, Vol. II: Nuclear Deformation* (W. A. Benjamin, Reading, MA, 1975).

[75] A. Staszczak, M. Stoitsov, A. Baran, and W. Nazarewicz, Augmented Lagrangian method for constrained nuclear density functional theory, Eur. Phys. J. A **46**, 85 (2010).

[76] T. R. Rodríguez, J. L. Egido, and L. M. Robledo, Phys. Rev. C **72**, 064303 (2005).

[77] J. Ripoche, T. Duguet, J.-P. Ebran, and D. Lacroix, Combining symmetry breaking and restoration with configuration interaction: extension to z-signature symmetry in the case of the Lipkin Model, Phys. Rev. C **97**, 064316 (2018).

[78] P. Ring and P. Schuck, *The Nuclear Many-Body Problem* (Springer, Heidelberg, 1980).

[79] C. A. Jiménez-Hoyos, T. M. Henderson, T. Tsuchimochi, and G. E. Scuseria, Projected Hartree–Fock theory, J. Chem. Phys. **136**, 164109 (2012).

[80] J. Ripoche, A. Tichai, and T. Duguet, Normal-ordered k-body approximation in particle-number-breaking theories, Eur. Phys. J. A **56**, 40 (2020).

[81] M. Frosini, T. Duguet, B. Bally, Y. Beaujeault-Taudière, J. P. Ebran, and V. Somà, In-medium k-body reduction of n-body operators: A flexible symmetry-conserving approach based on the sole one-body density matrix, Eur. Phys. J. A **57**, 151 (2021).

[82] G. Hagen, T. Papenbrock, D. J. Dean, A. Schwenk, A. Nogga, M. Włoch, and P. Piecuch, Coupled-cluster theory for three-body Hamiltonians, Phys. Rev. C **76**, 034302 (2007).

[83] R. Roth, S. Binder, K. Vobig, A. Calci, J. Langhammer, and P. Navrátil, Medium-Mass Nuclei with Normal-Ordered Chiral $NN+3N$ Interactions, Phys. Rev. Lett. **109**, 052501 (2012).

[84] I. Shavitt and R. J. Bartlett, *Many-body Methods in Chemistry and Physics* (Cambridge University Press, Cambridge, UK, 2009).

[85] A. Tichai, J. Müller, K. Vobig, and R. Roth, Natural orbitals for *ab initio* no-core shell model calculations, Phys. Rev. C **99**, 034321 (2019).

[86] J. Hoppe, A. Tichai, M. Heinz, K. Hebeler, and A. Schwenk, Natural orbitals for many-body expansion methods, Phys. Rev. C **103**, 014321 (2021).

[87] M. Kortelainen, Z. Sun, G. Hagen, W. Nazarewicz, T. Papenbrock, and P.-G. Reinhard, Universal trend of charge radii of even-even Ca-Zn nuclei, Phys. Rev. C **105**, L021303 (2022).

[88] D. A. Varshalovich, A. N. Moskalev, and V. K. Khersonskii, *Quantum Theory of Angular Momentum* (World Scientific, Singapore, 1988).

[89] D. J. Thouless, Stability conditions and nuclear rotations in the Hartree-Fock theory, Nucl. Phys. **21**, 225 (1960).

[90] C. Wa Wong, Generator-coordinate methods in nuclear physics, Phys. Rep. **15**, 283 (1975).

[91] R. A. Broglia, J. Terasaki, and N. Giovanardi, The Anderson-Goldstone-Nambu mode in finite and in infinite systems, Phys. Rep. **335**, 1 (2000).

[92] C. Yannouleas and U. Landman, Symmetry breaking and quantum correlations in finite systems: Studies of quantum dots and ultracold Bose gases and related nuclear and chemical methods, Rep. Prog. Phys. **70**, 2067 (2007).

[93] M. Deserno, How to generate equidistributed points on the surface of a sphere, 2004 (unpublished), https://www.cmu.edu/biolphys/deserno/pdf/sphere_equi.pdf.

[94] S. Weinberg, *The Quantum Theory of Fields* (Cambridge University Press, Cambridge, UK, 1996), Vol. II.

[95] T. Papenbrock and H. A. Weidenmüller, Effective field theory for finite systems with spontaneously broken symmetry, Phys. Rev. C **89**, 014334 (2014).

[96] R. E. Peierls and J. Yoccoz, The collective model of nuclear motion, Proc. Phys. Soc. A **70**, 381 (1957).

[97] M. R. Schindler and D. R. Phillips, Bayesian methods for parameter estimation in effective field theories, Ann. Phys. (NY) **324**, 682 (2009).

[98] R. J. Furnstahl, D. R. Phillips, and S. Wesolowski, A recipe for EFT uncertainty quantification in nuclear physics, J. Phys. G: Nucl. Part. Phys. **42**, 034028 (2015).

[99] E. A. Coello Pérez and T. Papenbrock, Effective field theory for nuclear vibrations with quantified uncertainties, Phys. Rev. C **92**, 064309 (2015).

[100] K. E. G. Löbner, M. Vetter, and V. Hönig, Nuclear intrinsic quadrupole moments and deformation parameters, At. Data Nucl. Data Tables **7**, 495 (1970).

[101] T. Dytrych, A. C. Hayes, K. D. Launey, J. P. Draayer, P. Maris, J. P. Vary, D. Langr, and T. Oberhuber, Electron-scattering form factors for ^{6}Li in the *ab initio* symmetry-guided framework, Phys. Rev. C **91**, 024326 (2015).

[102] R. Kanungo, W. Horiuchi, G. Hagen, G. R. Jansen, P. Navratil, F. Ameil, J. Atkinson, Y. Ayyad, D. Cortina-Gil, I. Dillmann, A. Estradé, A. Evdokimov, F. Farinon, H. Geissel, G. Guastalla, R. Janik, M. Kimura, R. Knöbel, J. Kurcewicz, Yu. A. Litvinov *et al.*, Proton Distribution Radii of $^{12-19}$C Illuminate Features of Neutron Halos, Phys. Rev. Lett. **117**, 102501 (2016).

[103] T. Duguet, V. Somà, S. Lecluse, C. Barbieri, and P. Navrátil, *Ab initio* calculation of the potential bubble nucleus ^{34}Si, Phys. Rev. C **95**, 034319 (2017).

[104] M. Burrows, R. B. Baker, Ch. Elster, S. P. Weppner, K. D. Launey, P. Maris, and G. Popa, *Ab initio* leading order effective potentials for elastic nucleon-nucleus scattering, Phys. Rev. C **102**, 034606 (2020).

[105] D. M. Brink and R. A. Broglia, *Nuclear Superfluidity* (Cambridge University Press, Cambridge, UK, 2005).

[106] A. Ekström, G. Baardsen, C. Forssén, G. Hagen, M. Hjorth-Jensen, G. R. Jansen, R. Machleidt, W. Nazarewicz, T. Papenbrock, J. Sarich, and S. M. Wild, Optimized Chiral Nucleon-Nucleon Interaction at Next-to-Next-to-Leading Order, Phys. Rev. Lett. **110**, 192502 (2013).

[107] G. Hagen, T. Papenbrock, and D. J. Dean, Solution of the Center-Of-Mass Problem in Nuclear Structure Calculations, Phys. Rev. Lett. **103**, 062503 (2009).

[108] G. Hagen, T. Papenbrock, D. J. Dean, and M. Hjorth-Jensen, *Ab initio* coupled-cluster approach to nuclear structure with modern nucleon-nucleon interactions, Phys. Rev. C **82**, 034330 (2010).

[109] N. M. Parzuchowski, S. R. Stroberg, P. Navrátil, H. Hergert, and S. K. Bogner, *Ab initio* electromagnetic observables with the in-medium similarity renormalization group, Phys. Rev. C **96**, 034324 (2017).

[110] M. G. Mayer and J. H. D. Jensen, *Elementary Theory of Nuclear Shell Structure* (John Wiley & Sons, New York, 1955).

[111] Á. Koszorús, X. F. Yang, W. G. Jiang, S. J. Novario, S. W. Bai, J. Billowes, C. L. Binnersley, M. L. Bissell, T. E. Cocolios, B. S. Cooper, R. P. de Groote, A. Ekström, K. T. Flanagan, C. Forssén, S. Franchoo, R. F. Garcia Ruiz, F. P. Gustafsson, G. Hagen, G. R. Jansen, A. Kanellakopoulos *et al.*, Charge radii of exotic potassium isotopes challenge nuclear theory and the magic character of N = 32, Nat. Phys. **17**, 439 (2021).

[112] I. Angeli and K. P. Marinova, Table of experimental nuclear ground state charge radii: An update, At. Data Nucl. Data Tables **99**, 69 (2013).

[113] T. Motobayashi, Y. Ikeda, K. Ieki, M. Inoue, N. Iwasa, T. Kikuchi, M. Kurokawa, S. Moriya, S. Ogawa, H. Murakami, S. Shimoura, Y. Yanagisawa, T. Nakamura, Y. Watanabe, M. Ishihara, T. Teranishi, H. Okuno, and R. F. Casten, Large deformation of the very neutron-rich nucleus ^{32}Mg from intermediate-energy Coulomb excitation, Phys. Lett. B **346**, 9 (1995).

[114] T. Baumann, A. M. Amthor, D. Bazin, B. A. Brown, C. M. Folden, A. Gade, T. N. Ginter, M. Hausmann, M. Matos, D. J. Morrissey, M. Portillo, A. Schiller, B. M. Sherrill, A. Stolz, O. B. Tarasov, and M. Thoennessen, Discovery of ^{40}Mg and ^{42}Al suggests neutron drip-line slant towards heavier isotopes, Nature (London) **449**, 1022 (2007).

[115] H. L. Crawford, P. Fallon, A. O. Macchiavelli, P. Doornenbal, N. Aoi, F. Browne, C. M. Campbell, S. Chen, R. M. Clark, M. L. Cortés, M. Cromaz, E. Ideguchi, M. D. Jones, R. Kanungo, M. MacCormick, S. Momiyama, I. Murray, M. Niikura, S. Paschalis, M. Petri *et al.*, First Spectroscopy of the Near Drip-Line Nucleus ^{40}Mg, Phys. Rev. Lett. **122**, 052501 (2019).

[116] D. T. Yordanov, M. L. Bissell, K. Blaum, M. De Rydt, Ch. Geppert, M. Kowalska, J. Krämer, K. Kreim, A. Krieger, P. Lievens, T. Neff, R. Neugart, G. Neyens, W. Nörtershäuser, R. Sánchez, and P. Vingerhoets, Nuclear Charge Radii of $^{21-32}$Mg, Phys. Rev. Lett. **108**, 042504 (2012).

[117] K. Fossez, J. Rotureau, N. Michel, Q. Liu, and W. Nazarewicz, Single-particle and collective motion in unbound deformed ^{39}Mg, Phys. Rev. C **94**, 054302 (2016).

[118] N. Tsunoda, T. Otsuka, N. Shimizu, M. Hjorth-Jensen, K. Takayanagi, and T. Suzuki, Exotic neutron-rich medium-mass nuclei with realistic nuclear forces, Phys. Rev. C **95**, 021304(R) (2017).

[119] T. Miyagi, S. R. Stroberg, J. D. Holt, and N. Shimizu, *Ab initio* multishell valence-space Hamiltonians and the island of inversion, Phys. Rev. C **102**, 034320 (2020).

[120] E. K. Warburton, J. A. Becker, and B. A. Brown, Mass systematics for $A = 29$–44 nuclei: The deformed $A \sim 32$ region, Phys. Rev. C **41**, 1147 (1990).

[121] H. Iwasaki, T. Motobayashi, H. Sakurai, K. Yoneda, T. Gomi, N. Aoi, N. Fukuda, Z. Fülöp, U. Futakami, Z. Gacsi, Y. Higurashi, N. Imai, N. Iwasa, T. Kubo, M. Kunibu, M. Kurokawa, Z. Liu, T. Minemura, A. Saito, M. Serata *et al.*, Large collectivity of ^{34}Mg, Phys. Lett. B **522**, 227 (2001).

[122] J. A. Church, C. M. Campbell, D.-C. Dinca, J. Enders, A. Gade, T. Glasmacher, Z. Hu, R. V. F. Janssens, W. F. Mueller, H. Olliver, B. C. Perry, L. A. Riley, and K. L. Yurkewicz, Measurement of $E2$ transition strengths in ^{32,34}Mg, Phys. Rev. C **72**, 054320 (2005).

[123] Z. Elekes, Zs. Dombrádi, A. Saito, N. Aoi, H. Baba, K. Demichi, Zs. Fülöp, J. Gibelin, T. Gomi, H. Hasegawa, N. Imai, M. Ishihara, H. Iwasaki, S. Kanno, S. Kawai, T. Kishida, T. Kubo, K. Kurita, Y. Matsuyama, S. Michimasa *et al.*, Proton inelastic scattering studies at the borders of the "island of inversion": The ^{30,31}Na and ^{33,34}Mg case, Phys. Rev. C **73**, 044314 (2006).

[124] S. Michimasa, Y. Yanagisawa, K. Inafuku, N. Aoi, Z. Elekes, Zs. Fülöp, Y. Ichikawa, N. Iwasa, K. Kurita, M. Kurokawa,

T. Machida, T. Motobayashi, T. Nakamura, T. Nakabayashi, M. Notani, H. J. Ong, T. K. Onishi, H. Otsu, H. Sakurai, M. Shinohara *et al.*, Quadrupole collectivity in island-of-inversion nuclei ^{28,30}Ne and ^{34,36}Mg, Phys. Rev. C **89**, 054307 (2014).

[125] M. R. Strayer, W. H. Bassichis, and A. K. Kerman, Correlation effects in nuclear densities, Phys. Rev. C **8**, 1269 (1973).

[126] J. D. Watts and R. J. Bartlett, Economical triple excitation equation-of-motion coupled-cluster methods for excitation energies, Chem. Phys. Lett. **233**, 81 (1995).

[127] R. de Swiniarski, C. Glashausser, D. L. Hendrie, J. Sherman, A. D. Bacher, and E. A. McClatchie, Evidence for Y_4 Deformation in ^{20}Ne and other *s-d* Shell Nuclei, Phys. Rev. Lett. **23**, 317 (1969).

[128] B. Pritychenko, M. Birch, B. Singh, and M. Horoi, Tables of $E2$ transition probabilities from the first 2^+ states in even-even nuclei, At. Data Nucl. Data Tables **107**, 1 (2016).

[129] A. Poves and A. Zuker, Theoretical spectroscopy and the fp shell, Phys. Rep. **70**, 235 (1981).

[130] M. Horoi, J. R. Gour, M. Włoch, M. D. Lodriguito, B. A. Brown, and P. Piecuch, Coupled-Cluster and Configuration-Interaction Calculations for Heavy Nuclei, Phys. Rev. Lett. **98**, 112501 (2007).

[131] S. Novario, P. Gysbers, J. Engel, G. Hagen, G. R. Jansen, T. D. Morris, P. Navrátil, T. Papenbrock, and S. Quaglioni, Coupled-Cluster Calculations of Neutrinoless Double-β Decay in ^{48}Ca, Phys. Rev. Lett. **126**, 182502 (2021).

[132] http://energy.gov/downloads/doe-public-access-plan.